

**FINAL REPORT: FA9550-07-1-0136, Dec. 2006 – Nov. 2009**

**Development of Non-Equilibrium Plasma-Flame Kinetic Mechanism and its Validation  
Using Gliding Arc Integrated with Counterflow Burner**

Principle Investigator: Yiguang Ju  
Department of Mechanical and Aerospace Engineering  
Princeton University  
D330, Engineering Quadrangle, Olden Street  
Princeton, NJ 08544  
E-mail: [yju@princeton.edu](mailto:yju@princeton.edu)  
Phone: 609-258-5644, Fax: 609-258-6233

Grant Number: **FA9550-07-1-0136**

Program Manager: Dr. Julian M. Tishkoff

Research Period: Dec. 2006 – Nov. 2009  
Report date: Feb. 21<sup>st</sup>, 2010

Report Documentation Page			Form Approved OMB No. 0704-0188		
Public reporting burden for the collection of information is estimated to average 1 hour per response, including the time for reviewing instructions, searching existing data sources, gathering and maintaining the data needed, and completing and reviewing the collection of information. Send comments regarding this burden estimate or any other aspect of this collection of information, including suggestions for reducing this burden, to Washington Headquarters Services, Directorate for Information Operations and Reports, 1215 Jefferson Davis Highway, Suite 1204, Arlington VA 22202-4302. Respondents should be aware that notwithstanding any other provision of law, no person shall be subject to a penalty for failing to comply with a collection of information if it does not display a currently valid OMB control number.					
1. REPORT DATE <b>21 FEB 2010</b>		2. REPORT TYPE <b>Final</b>		3. DATES COVERED <b>01-12-2006 to 30-11-2009</b>	
4. TITLE AND SUBTITLE <b>(U) Development of Non-Equilibrium Plasma-Flame Kinetic Mechanism and its Validation Using Gliding Arc Integrated with Counterflow Burner</b>				5a. CONTRACT NUMBER <b>FA9550-07-1-0136</b>	
				5b. GRANT NUMBER	
				5c. PROGRAM ELEMENT NUMBER	
6. AUTHOR(S) <b>Yiguang Ju ; Timothy Ombrello; Alexander Fridman</b>				5d. PROJECT NUMBER	
				5e. TASK NUMBER	
				5f. WORK UNIT NUMBER	
7. PERFORMING ORGANIZATION NAME(S) AND ADDRESS(ES) <b>Princeton University, Department of Mechanical and Aerospace Engineering, EQUAD on Olden Street, Princeton, NJ, 08544</b>				8. PERFORMING ORGANIZATION REPORT NUMBER <b>; AFRL-OSR-VA-TR-2011-0253</b>	
9. SPONSORING/MONITORING AGENCY NAME(S) AND ADDRESS(ES) <b>AFOSR, 875 North Randolph Street, Suite 325, Arlington, VA, 22203</b>				10. SPONSOR/MONITOR'S ACRONYM(S)	
				11. SPONSOR/MONITOR'S REPORT NUMBER(S) <b>AFRL-OSR-VA-TR-2011-0253</b>	
12. DISTRIBUTION/AVAILABILITY STATEMENT <b>Approved for public release; distribution unlimited</b>					
13. SUPPLEMENTARY NOTES					
14. ABSTRACT <b>Kinetic enhancements of NO<sub>x</sub>, O<sub>3</sub>, and O<sub>2</sub>(a1&amp;#916;g) on ignition and flame propagation of CH<sub>4</sub> and H<sub>2</sub>, C<sub>3</sub>H<sub>8</sub> and C<sub>2</sub>H<sub>4</sub> flames by non-equilibrium plasma discharges in air were studied experimentally. The important kinetic enhancement pathways were identified. It was found that plasma produced NO<sub>x</sub> played a dominant role in the reduction of ignition temperature, particularly at low temperatures and low stretch rates. Moreover, the results showed that NO<sub>x</sub> catalytic effect mitigated the inhibiting effects of H<sub>2</sub>O and CH<sub>4</sub> on ignition. A new method to isolate the kinetic coupling of O<sub>3</sub> and O<sub>2</sub>(a1&amp;#916;g) was proposed and the kinetic enhancement of O<sub>3</sub> and O<sub>2</sub>(a1&amp;#916;g) on flame speed was investigated quantitatively by using a lifted flame and advanced absorption and cavity ring down spectroscopy. It was found that O<sub>3</sub> decomposition in the early stages of the preheating zone produced atomic O which reacted rapidly with the fuel to extract chemical heat release to increase flame speed. It was also found that O<sub>2</sub>(a1&amp;#916;g) formation enhance combustion considerably via H+ O<sub>2</sub>(a1&amp;#916;g)=OH+O chain-branching reaction. The results will have a direct impact on the development of detailed plasma-flame kinetic mechanisms.</b>					
15. SUBJECT TERMS <b>Non-equilibrium plasma assisted combustion, Singlet oxygen, Ozone, NO<sub>x</sub>, Counterflow flame, Lifted flame</b>					
16. SECURITY CLASSIFICATION OF:			17. LIMITATION OF ABSTRACT <b>Same as Report (SAR)</b>	18. NUMBER OF PAGES <b>49</b>	19a. NAME OF RESPONSIBLE PERSON
a. REPORT <b>unclassified</b>	b. ABSTRACT <b>unclassified</b>	c. THIS PAGE <b>unclassified</b>			



## Table of Contents

<b>Abstract .....</b>	<b>2</b>
<b>1.0 Introduction.....</b>	<b>3</b>
<b>2.0 Experimental Methods and Results of Non-Equilibrium Plasma-assisted Combustion ..</b>	<b>6</b>
2.1 NO <sub>x</sub> Catalytic Effects on Ignition Enhancement with Magnetic Gliding Arc (MGA) .....	6
2.1.1 <i>Experimental System and Methods</i> .....	6
2.1.2. <i>Computational Methods</i> .....	8
2.1.3. <i>Results and Discussion</i> .....	8
2.1.4. <i>Conclusions</i> .....	13
2.2 Flame Propagation Enhancement by Plasma Generated O <sub>3</sub> .....	14
2.2.1 <i>Experimental System and Methods</i> .....	14
2.2.2 <i>Quantitative Absorption Measurements of O<sub>3</sub></i> .....	16
2.2.3. <i>Results and Discussion</i> .....	17
2.2.4. <i>Conclusions</i> .....	25
2.3 Flame Propagation Enhancement by Plasma Generated O <sub>2</sub> (a <sup>1</sup> Δ <sub>g</sub> ).....	26
2.3.1 <i>Experimental System</i> .....	26
2.3.2 <i>Results and Discussion</i> .....	31
2.3.3 <i>Conclusions</i> .....	41
<b>3.0 Participating Personnel.....</b>	<b>42</b>
<b>4.0 Publications .....</b>	<b>43</b>
<i>Peer Reviewed Journal Publications</i> .....	43
<i>Presentations at Conferences</i> .....	43
<b>5.0 Interactions and Consultations .....</b>	<b>44</b>
<b>6.0 Honors and Awards.....</b>	<b>44</b>
<b>7.0 Inventions.....</b>	<b>44</b>
<b>8.0 References of This Report .....</b>	<b>45</b>

## Abstract

Kinetic enhancements of  $\text{NO}_x$ ,  $\text{O}_3$ , and  $\text{O}_2(\text{a}^1\Delta_g)$  on ignition and flame propagation of  $\text{CH}_4$  and  $\text{H}_2$ ,  $\text{C}_3\text{H}_8$ , and  $\text{C}_2\text{H}_4$  flames by non-equilibrium plasma discharges in air were studied experimentally. The important kinetic enhancement pathways were identified. Plasma-produced  $\text{NO}_x$  played a dominant role in the reduction of ignition temperature particularly at low temperatures and low stretch rates; moreover, the results showed that  $\text{NO}_x$  catalytic effect mitigated the inhibiting effects of  $\text{H}_2\text{O}$  and  $\text{CH}_4$  on ignition. A new method to isolate the kinetic coupling of  $\text{O}_3$  and  $\text{O}_2(\text{a}^1\Delta_g)$  was proposed, and the kinetic enhancement of  $\text{O}_3$  and  $\text{O}_2(\text{a}^1\Delta_g)$  on flame speed was investigated quantitatively by using a lifted flame and advanced absorption and cavity ring down spectroscopy.  $\text{O}_3$  decomposition in the early stages of the preheating zone produced atomic O which reacted rapidly with the fuel to extract chemical heat release to increase flame speed. Also,  $\text{O}_2(\text{a}^1\Delta_g)$  formation enhanced combustion considerably via the  $\text{H} + \text{O}_2(\text{a}^1\Delta_g) = \text{OH} + \text{O}$  chain-branching reaction. The results will have a direct impact on the development of detailed plasma-flame kinetic mechanisms.

## 1.0 Introduction

The development of high-speed air-breathing propulsion vehicles with scramjet engines has created the challenges of achieving efficient and reliable ignition, flame propagation, and flame stabilization. Particularly, when hydrocarbon fuels are used, the flow residence time is comparable to the chemical reaction time, and ignition and flame stabilization become extremely difficult; therefore, the development of new methods to decrease ignition delay time and to increase flame stabilization and flame propagation rates is critical for the development of vehicles capable of hypersonic flight.

One of the potential solutions to enhance combustion and chemical reactions is the application of plasma activation. Plasma-assisted combustion produces elevated temperatures, radicals, excited species, ions, and electrons that have the possibility to increase the rate of fuel oxidation. Because of the significant promise of plasmas, extensive research has been performed using a variety of plasma discharge systems, including plasma torches/jets [1,2,3,4], gliding arc discharges [5,6,7], fast ionization waves [8, 9], and nanosecond repetitively pulsed discharges [10, 11], as well as through electric field interactions [12,13,14,] and microwave discharges [15,16,17]. The investigations have shown that plasma can enhance combustion processes with decreased ignition time and lower ignition temperatures [6,7,10,11,18,19], increased flame propagation [13,14,16,17,20], and enhanced flame stabilization [2,3,7,15]. Despite many observations of plasma-assisted combustion, due to the complex kinetic and transport interaction there is a lack of data from controlled and well-defined experiments to advance the fundamental understanding of the kinetic processes [21].

One of the major challenges associated with understanding the plasma-flame interaction is to establish a well-defined experimental system to achieve the isolation of the effects of individual species and to gain a fundamental knowledge of specific enhancement processes. Plasma discharges can produce a wide range of stable and metastable species that have the potential to enhance combustion, especially when the discharge is in a premixture of fuel and oxidizer. There is a lack of understanding of what species and reaction pathways are the most important.

**Figure 1** is an illustration of typical plasma-produced species and their lifetimes as a function of pressure in different engines. Depending upon the application and the species of interest, decoupling the plasma-flame interactions can be very challenging. For example, when the pressure is sufficiently low (sub-atmospheric), plasma-produced species have high mole fractions and long lifetimes. On the other hand, at extremely high pressures, plasma-produced species have very short lifetimes because of high rates of recombination and collisional quenching.

Since the concentration of species is proportional to the pressure and hence the number density, the lower the pressure, the longer the mean free path and the lower the collision frequency. To minimize the loss of radicals and excited species, the pressures need to be low or the plasma discharge has to be created at the reaction zone to enhance combustion. Unfortunately, decoupling of the plasma-combustion interactions becomes increasingly difficult as the plasma

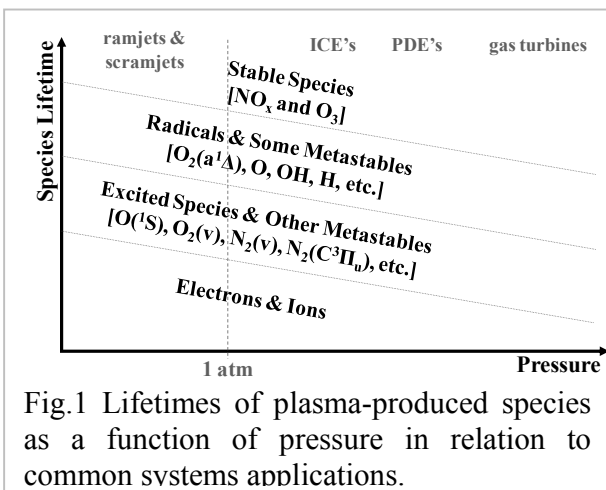


Fig.1 Lifetimes of plasma-produced species as a function of pressure in relation to common systems applications.

discharge is moved closer to the reaction zone. In addition, diagnostics of plasma-generated species in reaction zone is challenging. These complications make it difficult to elucidate the fundamental interactions, especially when trying to understand the effects of specific plasma-produced species.

Plasmas generate electrons, ions, excited species, radicals, and fuel fragments. The role of active radicals in combustion and plasma-assisted combustion has been studied extensively [19, 22]; however, the effects of long lifetime excited and intermediate species such as  $\text{NO}_x$ ,  $\text{O}_3$  and  $\text{O}_2(\text{a}^1\Delta_g)$  are not well understood despite their great importance in affecting plasma-assisted combustion processes. The focus of this project is to understand the kinetic pathways of these species in affecting ignition and flame propagation of hydrocarbon fuels.

For the study of plasma generated  $\text{NO}_x$  effects on combustion, the extinction and ignition enhancements by  $\text{NO}_x$  on hydrogen and methane diffusion flames were investigated by the PI using a counterflow flame integrated with a gliding arc [5, 6]. The results showed that plasma has a significant effect on the extension of the extinction limit; however, due to the fast recombination of radicals and the rich radical pool in flames, the effect of the plasma on flame extinction was predominately thermal. Experiments on hydrogen and methane ignition with plasma discharge in air demonstrated successfully that the production of  $\text{NO}$  in plasma reduced ignition temperature dramatically. Nevertheless, in practical combustion systems plasma discharges occur often under partially premixed conditions. As such, a question of how the kinetic inhibition of  $\text{H}_2\text{O}$  and  $\text{CO}_2$  affects  $\text{NO}$  catalytic effects arises; therefore, the **first goal** of our research is to develop a simplified experimental apparatus to study partially premixed ignition in a plasma-flame system and use computational simulations to gain insight into the mechanisms of  $\text{NO}$  enhancement effects with the appearance of kinetic inhibition of  $\text{H}_2\text{O}$  and  $\text{CO}_2$ . A new experimental system was developed to study the non-thermal ignition of simple fueled ( $\text{H}_2$ - $\text{CH}_4$ -air) counterflow diffusion flames by a non-equilibrium magnetic gliding arc (MGA) plasma discharge. Ignition temperatures were measured experimentally using air and ultra-lean pre-mixtures with  $\text{H}_2$  and  $\text{CH}_4$ , and the concentrations of stable plasma-produced species were measured using an FT-IR spectrometer. These results were used, along with computational simulations, to identify some of the key species of non-thermal ignition enhancement in the plasma-flame system.

For the study of  $\text{O}_3$  effects on combustion, there has been little experimental work emphasizing the combustion enhancement effects of  $\text{O}_3$ . Early experimental studies of the effects of  $\text{O}_3$  on ignition delay times were conducted in compression and spark ignition engines [23,24,25,26,27]. Recently, laser ignition was investigated by using both  $\text{CO}_2$  and  $\text{KrF}$  excimer lasers to excite and decompose  $\text{O}_3$  [28,29,30]. To the authors' knowledge, there have only been two investigations of the effect of  $\text{O}_3$  on flame propagation enhancement [25, 31]. Although these experiments reported flame speed enhancement by  $\text{O}_3$ , the exact mechanisms are not well understood. Moreover, quantification of the enhancement was difficult due to the complex experimental geometry; therefore, the **second goal** of the present work is to create a methodology to measure quantitatively the effects of plasma-generated  $\text{O}_3$  on the enhancement of flame propagation at a pressure of 1 atm. In this project, the enhancement of flame propagation of  $\text{C}_3\text{H}_8$  lifted flames by  $\text{O}_3$  was investigated through the development of an integrated plasma-combustion experimental platform where the active species were produced, isolated, and transported, and quantitative measurements of  $\text{O}_3$  were conducted by using absorption spectroscopy. The experimental results were compared to numerical simulations to

identify the important kinetic pathways of flame propagation enhancement in the plasma-flame systems.

Singlet delta oxygen,  $O_2(a^1\Delta_g)$ , which has a low excitation energy of 0.98 eV and long radiative lifetime ( $>4000$  s) because of a spin-forbidden transition to the ground state [32], has attracted much attention because of the faster chain-branching rate of  $H+O_2(a^1\Delta_g)$  than that of  $H+O_2$ . There have been numerous computational studies aimed to quantify the enhancement of ignition and flame stabilization by  $O_2(a^1\Delta_g)$ . Starik and Titova [33] showed that when  $O_2$  was excited to its first electronic state of  $O_2(a^1\Delta_g)$  by laser radiation in a supersonic flow of  $H_2$ -air, the induction time and temperatures necessary for ignition behind a shockwave were reduced significantly. They attributed the enhancement to come from new pathways with  $O_2(a^1\Delta_g)$  to generate active species, such as O, H, and OH. Numerical simulations also were performed to demonstrate similar effects of  $O_2(a^1\Delta_g)$  using an electrical discharge [34]. Detailed investigations of the ignition kinetics with the presence of  $O_2(a^1\Delta_g)$  by non-equilibrium excitation in a  $H_2$ - $O_2$  system was reviewed by Popov [35]. The review pointed out that if the quenching of  $O_2(a^1\Delta_g)$  by  $H_2$  is not considered, there will be a gross overestimate of the amount of enhancement because the collisional quenching rate increases significantly with temperature. Popov also emphasized that there is a lack of experimental studies of the effect of electronically excited species on combustion phenomena.

Starik, Kuleshov, and Titova studied the ignition enhancement of  $O_2(a^1\Delta_g)$  and  $O(^1D)$  in an  $H_2$ - $O_2$  mixture. The collective effect of these two species led to decreased ignition delay times by several orders of magnitude [36]. Kozlov, Starik, and Titova also conducted numerical simulations on ignition to show the enhancement of  $H_2$ - $O_2$  flame speed with  $O_2(a^1\Delta_g)$  addition [37]. The results showed that a concentration of 10%  $O_2(a^1\Delta_g)$  gave more than a 50% increase in the laminar flame velocity. Bourig et al. [38] extended the numerical modeling by investigating ignition and flame propagation, as well as flame stabilization by  $O_2(a^1\Delta_g)$ . Experimental validation of the enhancement of  $O_2(a^1\Delta_g)$  on ignition was introduced by measurement of the emission from  $OH^*$  at 306.4 nm [39]. The results of  $OH^*$  measurements confirmed the kinetic enhancement by  $O_2(a^1\Delta_g)$ . Skrebkov and Karkach [40] performed subsequent simulations using the ignition and emission spectroscopy results and showed that there was reasonable agreement; however, they emphasized that the main stumbling block was the “availability of experimentally evaluated amounts of  $O_2(a^1\Delta_g)$ ” [41].

To date, there has only been one experimental investigation of the effects of  $O_2(a^1\Delta_g)$  on combustion phenomena. Smirnov et al. [42] performed experiments aimed at isolating the effect of  $O_2(a^1\Delta_g)$  on the ignition of  $H_2$ - $O_2$ -He mixtures at low pressure between 1.33 kPa and 2.67 kPa. The results showed decreased induction times. In order to isolate the effect of O and  $O_3$ , Hg and its oxide (HgO) were injected into the flow; however, the concentration of  $O_3$  was not measured, and  $O_2(a^1\Delta_g)$  was measured only through emission intensity. The measurements did not provide quantitative concentrations of all the major species of enhancement in the system, although it was the first attempt to isolate the effect of  $O_2(a^1\Delta_g)$  and the results agreed reasonably well with their previous calculations [43,44]. In addition, the experiments were conducted only for a  $H_2$ - $O_2$  mixture. Collision quenching of  $O_2(a^1\Delta_g)$  by hydrocarbon molecules were not considered; therefore, there are scarce experimental data quantifying the effect of electronically excited species, specifically  $O_2(a^1\Delta_g)$ , on combustion phenomena. A majority of the numerical and experimental work has been focused on the  $H_2$ - $O_2$  reaction system, with no experimental studies of the isolated effects of  $O_2(a^1\Delta_g)$  on hydrocarbon based fuels; moreover, there have been no experimental studies at higher pressures, greater than 2.67 kPa, where a structured flame can



exist. Furthermore, there have been no experimental studies with quantitative and simultaneous concentration measurements of  $O_2(a^1\Delta_g)$ , O,  $O_3$ , and NO.

The **third goal** of the present work is to isolate and measure quantitatively the effects of  $O_2(a^1\Delta_g)$  on the enhancement of flame propagation using a hydrocarbon-based fuel, as well as to understand the kinetic mechanisms involved. The enhancement of flame propagation speeds was investigated through the development of an integrated plasma combustion experimental platform, and absolute concentration measurements were taken through integrated cavity output absorption spectroscopy. The experiments provided the first experimental evidence of the isolated effect of  $O_2(a^1\Delta_g)$  on the propagation of a hydrocarbon fuel-based flame. The results will provide important steps towards developing a comprehensive predictive model for plasma-combustion systems with detailed and well-defined experimental results.

## 2.0 Experimental Methods and Results of Non-Equilibrium Plasma-assisted Combustion

### 2.1 NOx Catalytic Effects on Ignition Enhancement with Magnetic Gliding Arc (MGA)

#### 2.1.1 Experimental System and Methods

In this experiment, we used the non-equilibrium Magnetic Gliding Arc (MGA) (**Fig.2**) developed in our previous studies [5,6] to produce NO<sub>x</sub>. The MGA is a special type of gliding arc discharge with non-equilibrium properties. The arc is established first as a thermal equilibrium plasma. It then elongates while it is rotated around by the Lorentz force from the magnetic field. During this process, the arc gains more non-equilibrium properties as it cools and more voltage is drawn from the power supply. The arc stabilizes and rotates at the largest gap along the electrodes, not reinitiating at the smallest gap because of passing through pre-ionized gas from the prior rotation. A time-integrated photo of the top of the MGA is shown in **Fig.2**. The benefit of the MGA is that it has both thermal equilibrium and non-equilibrium processes to produce heat, NO<sub>x</sub>, as well as radicals needed to enhance ignition in a combustion system.

The MGA was integrated with a counterflow ignition system (**Fig.3**) because of the counterflow's unique benefits of simplified flame geometry, minimal buoyancy effects, and the ability to define a strain rate,  $a_i$ , (flow velocity gradient or inverse of residence time) on the centerline near the stagnation plane of the two impinging jets. The strain rate is defined as,

$$a_i = \frac{2v_i}{L} \left( 1 + \frac{v_j}{v_i} \sqrt{\frac{\rho_j}{\rho_i}} \right) \quad (1)$$

where  $L$ ,  $v$  and  $\rho$  are the length between the two nozzles, velocity, and density, respectively, and  $i$  and  $j$  are indices representing the two nozzles streams. The strain rate was a parameter used for comparison to computational simulations. A schematic of the MGA plasma discharge counterflow ignition system is shown in **Fig.3**. The ignition apparatus consisted of two converging nozzles opposed to each other. The upper nozzle was water-cooled and was used for N<sub>2</sub>-diluted H<sub>2</sub>. The lower nozzle was preceded with a silicon carbide heater to pre-heat the air, a spacer where small concentrations of H<sub>2</sub> and CH<sub>4</sub> were injected into the air stream to create ultra-

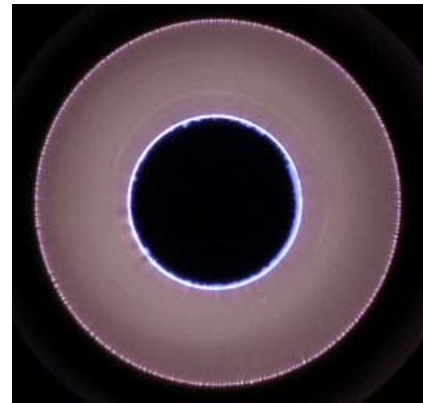


Fig.2 Time integrated photo of top view of MGA.

lean pre-mixtures, and finally the MGA plasma device. Both nozzles contained a  $N_2$  co-flow to isolate the flame from any ambient air and disturbances.

The entire system was designed to measure steady-state ignition temperatures with and without plasma activation of air or ultra-lean pre-mixtures. The temperature profiles across the exit of the lower nozzle were confirmed to be peaked along the centerline with no hot spots in the flow; therefore, the ignition temperatures were measured with two different diameter K-type thermocouples axially at the exit of the lower nozzle. The two thermocouples could be interchanged at the same location in the flow, allowing for more accurate radiation and conduction corrections.

To achieve ignition in the system, the temperature of the oxidizer side initially was raised close to the ignition temperature. The temperature then was increased slowly in small increments by approximately 2 K - 3 K until ignition was achieved by increasing the power supplied to the silicon carbide heater. The heater power at which ignition occurred was recorded, and the flame was extinguished by closing off the supply of fuel. The heater power then was lowered, the fuel turned on, and the flow field correctly adjusted and optimized again. The heater power again was increased, ignition achieved, and power recorded. Once the power at ignition was found several times to be consistently the same, the fuel supply was closed off and the heater adjusted to that power. The thermocouples were placed in the flow axially at the exit of the lower nozzle, and the temperature was measured. This measured temperature was defined as the ignition temperature, and the procedure was followed several times to establish repeatability.

Any difference in ignition temperatures between having the MGA plasma discharge on and off would be a non-thermal effect because of the minimization of all localized thermal effects. The experiment therefore provided a well-defined system to study non-thermal ignition enhancement by a non-equilibrium plasma.

The significant distance between the MGA and the reaction zone yielded long residence time which would suppress any effects of ions or excited species and would focus on and isolate the effects of stable plasma-produced species. To quantify the stable plasma-produced species that affected the ignition of the  $H_2$

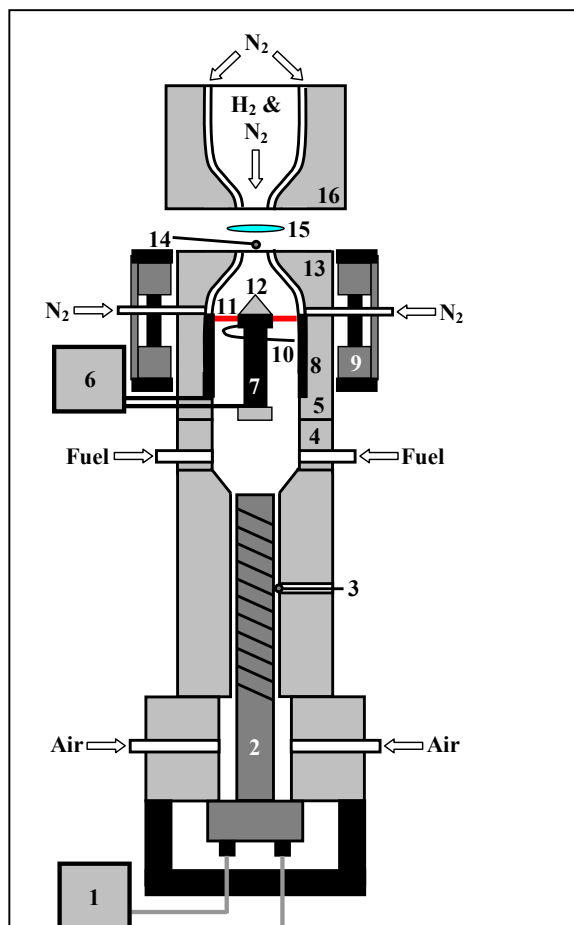


Fig.3 MGA Counterflow Ignition Apparatus 1. Silicon Controlled Rectifier, 2. Silicon carbide heater, 3. R-type thermocouple, 4. Fuel injection spacer 5. MGA plasma power supply, 6. MGA device, 7. Cathode, 8. Anode, 9. Magnets, 10. Gliding arc initiation wire, 11. MGA, 12. Insulator, 13. Nozzle with  $N_2$  co-flow, 14. K-type thermocouple, 15. Diffusion flame, 16. Water-cooled nozzle with  $N_2$  co-flow.

counterflow diffusion flames, a Fourier Transform Infrared (FT-IR) spectrometer was used. For accurate measurements of the stable species in the system, a 200 micron quartz probe was placed axially along the centerline at the exit of the lower nozzle where the thermocouples measured the peak temperature. The quartz probe was attached to the heated line of a Nicolet Magna-IR 550 Spectrometer. Pressure in the system was held constant at 336 Torr to ensure that the reactions would be quenched when pulled into the quartz sampling probe, as well as to maintain a high flow rate through the system to improve sampling time. The FT-IR was calibrated for six stable species which included CH<sub>4</sub>, CO, CO<sub>2</sub>, NO, NO<sub>2</sub> and H<sub>2</sub>O at the same conditions of the experiments and in the appropriate concentration ranges.

### 2.1.2. Computational Methods

To validate the experimental results and understand the underlying mechanisms of ignition enhancement by the MGA, computational simulations were performed. A code derived from the PI's previously developed code for counterflow flame simulations was used. The S-curve response was found for all experimental conditions using the geometry of the actual counterflow burner and the species present at the exit of the nozzles. For the fuel side (upper nozzle), the species concentrations were held constant at 20% H<sub>2</sub> in 80% N<sub>2</sub>, but for the oxidizer side (lower nozzle), the species ranged from a majority of air with 21% O<sub>2</sub> and 79% N<sub>2</sub> to small concentrations of plasma-produced species that were measured by the FT-IR, such as CH<sub>4</sub>, CO, CO<sub>2</sub>, NO, NO<sub>2</sub> and H<sub>2</sub>O. Detailed chemistry was used with the mechanism of Li et al. [45] (H<sub>2</sub>) and Mueller et al. [46] (NO<sub>x</sub>) for the ignition with air and with ultra-lean H<sub>2</sub> pre-mixtures for the oxidizer side of the counterflow system. To capture the ignition phenomena correctly when using ultra-lean CH<sub>4</sub> pre-mixtures for the oxidizer side, the dimethyl-ether (DME) mechanism of Zhao et al. [47] was used with the NO<sub>x</sub> of GRI-3.0 [48]. Zhao's DME mechanism aptly suited these cases because it had the H<sub>2</sub> sub-mechanism of Li et al., but also included CH<sub>4</sub> chemistry to capture the behavior of the species from the ultra-lean CH<sub>4</sub> mixtures. Furthermore, the DME mechanism of Zhao et al. had been validated by Zheng et al. for DME-blended CH<sub>4</sub>-air flames [49]. The flame temperature versus strain rate S-curves were computed for the experimental conditions, and the ignition temperatures were found as a function of strain rate.

To identify the key species and reactions that were influential at ignition, a sensitivity analysis was performed at the ignition turning point on the S-curve. The sensitivity coefficient was defined as

$$SC = \frac{\partial \ln(a_{\text{ignition}})}{\partial \ln(k_i)} \quad (2)$$

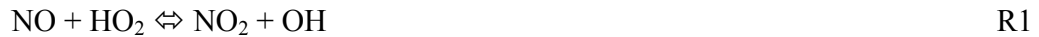
where  $a_{\text{ignition}}$  was the strain rate at ignition and  $k_i$  was the reaction rate of the  $i^{\text{th}}$  reaction. A positive sensitivity coefficient meant that increasing the reaction rate accelerated ignition and vice versa.

### 2.1.3. Results and Discussion

To establish first a baseline set of experimental data, measurements of the ignition temperatures of only air as the oxidizer for the MGA being on and off was found, and the results are shown in Fig.4. The ignition temperatures decreased dramatically when the MGA was activating the air, indicating that there was significant non-thermal ignition enhancement by the plasma.

Since the oxidizer was only air,  $\text{NO}_x$  would be one of the few stable species capable of decreasing the ignition temperature. Quantitative measurements of  $\text{NO}_x$  were made using the FT-IR at the exit of the lower nozzle. Large concentrations of  $\text{NO}_x$  were found, with approximately 3500 parts per million (ppm) of  $\text{NO}$  and 1300 ppm of  $\text{NO}_2$ . The  $\text{NO}_x$  concentrations were used as initial/boundary conditions on the oxidizer side of the computational simulations. The computed curves of air and air with  $\text{NO}_x$  are shown in Fig.4 with comparisons to the experimental results. There was good agreement when air was the oxidizer but an over-prediction of the enhancement by  $\text{NO}_x$ . The over-prediction was attributed to the fact that the  $\text{NO}_x$  input to the computation was only in the form of  $\text{NO}$ , not  $\text{NO}$  and  $\text{NO}_2$ . Since  $\text{NO}$  is a more effective catalyst than  $\text{NO}_2$  in the  $\text{NO}_x$  cycle, the introduction of only  $\text{NO}$  to the simulations would yield lower ignition temperatures and hence an over-estimate of the ignition enhancement, which was observed. Overall,  $\text{NO}_x$  was the primary means of enhancement when only air was activated by the MGA.

The results of a sensitivity analysis at the ignition turning points for the conditions of air and  $\text{NO}_x$  addition are shown in Fig.5. With the addition of  $\text{NO}_x$ , the ignition enhancement was from the catalytic role that the  $\text{NO}_x$  played on the oxidation of the inactive  $\text{HO}_2$  radical by the reaction of



with the replenishment of  $\text{NO}$  from  $\text{NO}_2$  coming mostly from the chain carrying reaction



and to a lesser extent by the reaction of



Figure 5 shows that there were other third body reactions that increased in importance with  $\text{NO}_x$  addition, but the net result was the conversion of  $\text{HO}_2$  to two  $\text{OH}$  radicals. To understand the effect of other plasma-produced species, ultra-lean pre-mixtures were chosen in place of air as the oxidizer on the  $\text{H}_2$  counterflow diffusion flames. The introduction of 1% and 2%  $\text{H}_2$ , as well as 0.2%, 0.5%, and 1%  $\text{CH}_4$  downstream of the heater and upstream of the MGA, allowed for homogeneous ultra-lean pre-mixtures that were activated by the MGA.

Initially, measurements of the ignition temperatures using the ultra-lean  $\text{H}_2$  pre-mixtures were taken and are shown in Fig. 4 compared to no fuel addition. With the progressive increase of  $\text{H}_2$  in the air, the ignition temperatures increased. Since the temperatures between the introduction of  $\text{H}_2$  to the air and the exit of the nozzle were on the order of 1000 K, a majority of

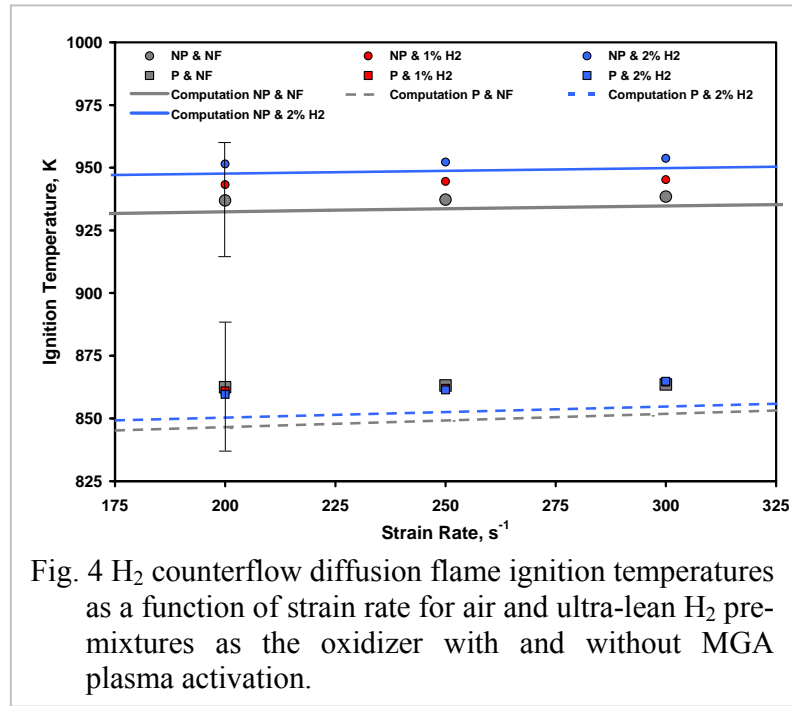


Fig. 4  $\text{H}_2$  counterflow diffusion flame ignition temperatures as a function of strain rate for air and ultra-lean  $\text{H}_2$  pre-mixtures as the oxidizer with and without MGA plasma activation.

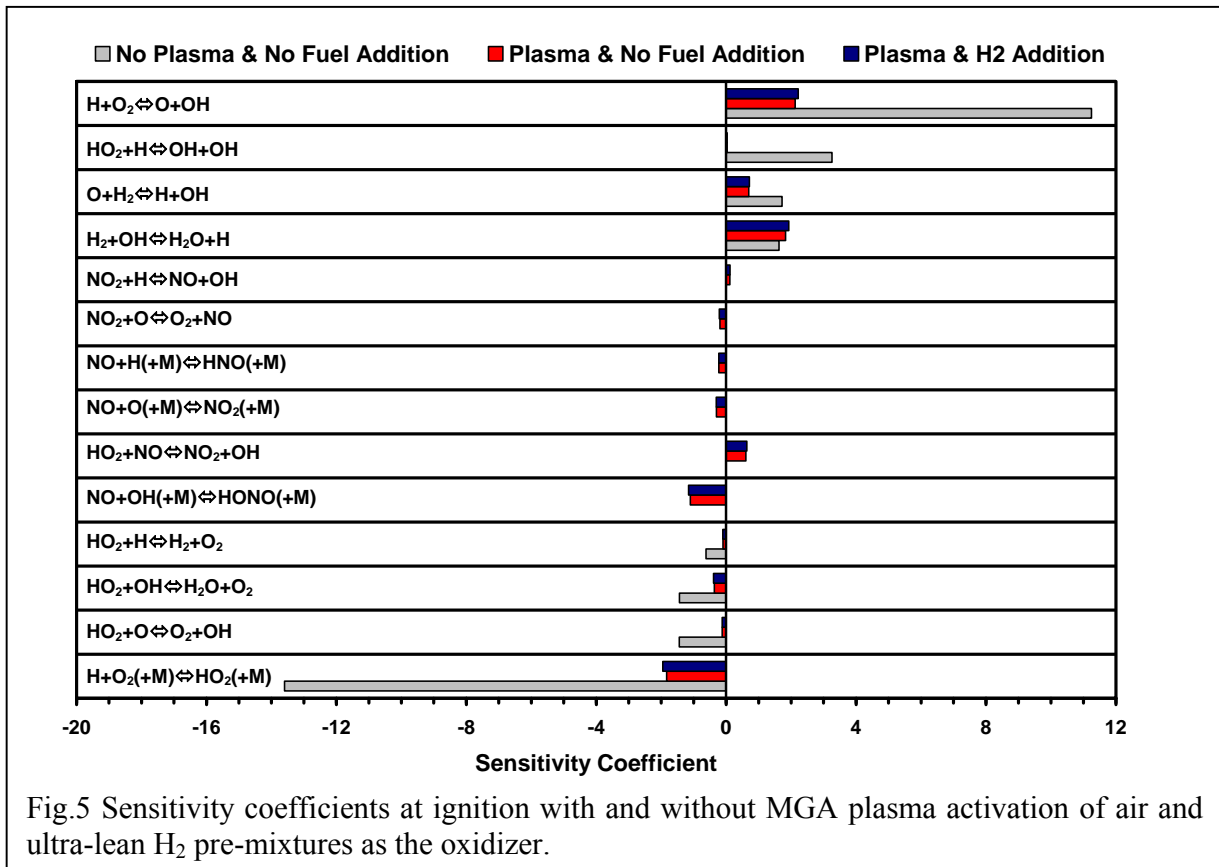
the  $H_2$  oxidized to  $H_2O$ . FT-IR spectrometer measurements confirmed that the majority of  $H_2$  was converted to  $H_2O$ . Since  $H_2O$  is a very effective third body in the reaction



converting the active  $H$  to  $HO_2$ , any  $H_2O$  present at the reaction zone would hinder ignition. Using the FT-IR spectrometer concentration measurements of  $H_2O$  in the counterflow code confirmed the ignition temperature rise, with good agreement to the experimentally measured temperatures (Fig. 4). Furthermore, the recent work of Langille et al. [50] showed similar results on counterflow  $H_2$ -air ignition using vitiated air. They found that for every 1% of  $H_2O$  addition there was approximately an 8 K rise in the ignition temperature, agreeing well with our results.

When the ultra-lean  $H_2$ -air pre-mixtures were activated by the MGA, the ignition temperatures did not change significantly from when only air was being activated. It was found by FT-IR spectrometer measurements that the concentration of  $H_2O$  at the exit of the lower nozzle decreased from that of no MGA activation; therefore, less  $H_2$  was oxidized to  $H_2O$ . Computational simulations agreed well with the experiments and showed no appreciable change in the ignition temperature with  $H_2$ -air pre-mixtures in place of only air. Sensitivity analysis at the ignition limit on the S-curve showed that there were competing effects at ignition (Fig. 5). Less  $H_2O$  yielded higher ignition temperatures, but the significant concentrations of  $NO_x$  produced by the plasma oxidized the  $HO_2$  (reaction R1) produced by the third body reaction, R4. Overall, the net effect was no significant change in the ignition temperature, which agreed well with the experimental results.

The most important result from using ultra-lean  $H_2$ -air pre-mixtures was that  $H_2O$  was a significant inhibitor of ignition, but when the MGA plasma activated the ultra-lean pre-mixtures,



the effect was mitigated because of the  $\text{NO}_x$  production. Furthermore, the thermal oxidation in the oxidizer stream, which was the case for no MGA activation, the flow residence times and temperatures were crucial for any change in the chemical composition of the gas. When the MGA was used, the residence times and high temperatures were both lower, but significant conversion of the fuel was achieved. The results demonstrated the unique benefit of using a non-equilibrium plasma to create species for ignition enhancement and mitigate the effect of  $\text{H}_2\text{O}$ .

Different behavior was observed when using ultra-lean  $\text{CH}_4$ -air pre-mixtures for the oxidizer side of the  $\text{H}_2$  counterflow diffusion flame ignition system. Firstly, for no MGA activation at low strain rates ( $a = 200 \text{ s}^{-1}$ ) the ignition temperatures increased much less than at higher strain rates (Fig.6). Unlike  $\text{H}_2$ , the flow residence times between the introduction of  $\text{CH}_4$  to the air stream and the reaction zone were on the order of the ignition delay times of  $\text{CH}_4$  at the associated gas temperatures. At low strain rates, there was sufficient time to oxidize fully the  $\text{CH}_4$  to  $\text{CO}_2$  and  $\text{H}_2\text{O}$ . FT-IR spectrometer measurements further confirmed the full oxidation of  $\text{CH}_4$ . In addition, numerical simulations showed that the majority of the ignition inhibition came

from  $\text{H}_2\text{O}$  with  $\text{CO}_2$ . The residence time somewhere between the strain rates of  $200 \text{ s}^{-1}$  and  $250 \text{ s}^{-1}$  was on the order of the ignition delay time of  $\text{CH}_4$  because more for the same amount of  $\text{CH}_4$  addition, the ignition temperatures increased more at higher strain rates. To show this clearly, a dotted line was used to connect the computational results at the strain rates of  $200 \text{ s}^{-1}$  and  $250 \text{ s}^{-1}$  (Fig.6). The FT-IR spectrometer measurements confirmed that only a portion of the  $\text{CH}_4$  was oxidized, with significant concentrations of  $\text{CO}$ ,  $\text{CO}_2$  and  $\text{H}_2\text{O}$  also present.

When the concentrations from the experiments were used as inputs to the computations, there was good agreement with the measured ignition temperatures. A sensitivity analysis (Fig.7) showed that the significant increase in the ignition temperature was due predominately to the un-oxidized  $\text{CH}_4$  converting the active  $\text{OH}$  radicals to  $\text{H}_2\text{O}$  through the reaction



Other reactions of  $\text{CH}_4$  and  $\text{CH}_3$  with  $\text{O}$  and  $\text{H}$  competed with the branching reactions for  $\text{H}_2$  oxidation of



to inhibit ignition but were far less important than reaction R5.

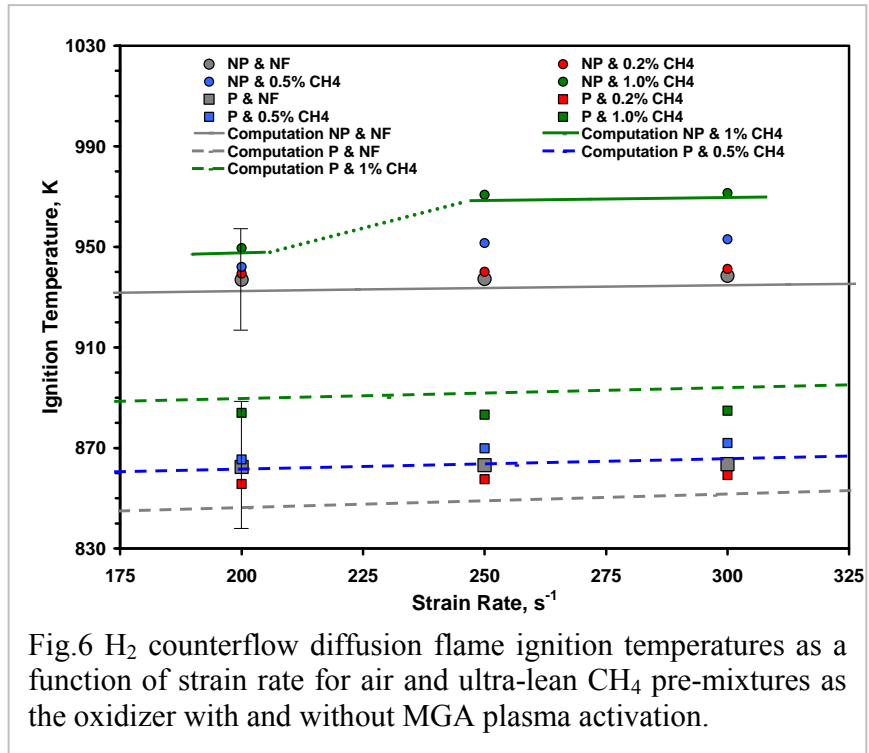


Fig.6  $\text{H}_2$  counterflow diffusion flame ignition temperatures as a function of strain rate for air and ultra-lean  $\text{CH}_4$  pre-mixtures as the oxidizer with and without MGA plasma activation.



Unlike the MGA activated ultra-lean  $H_2$  pre-mixtures, there was a significant change in the ignition temperatures for the MGA activated ultra-lean  $CH_4$  pre-mixtures. The experimentally measured ignition temperatures are shown in Fig.6. There was a non-monotonic behavior observed with the increase of  $CH_4$  in the oxidizer. The ignition temperatures decreased first with 0.2%  $CH_4$  addition and then increased with 0.5% and 1%  $CH_4$  addition to the oxidizer. To examine and understand the differences in ignition behavior, FT-IR spectrometer measurements of  $CH_4$ ,  $CO$ ,  $CO_2$ ,  $NO$ ,  $NO_2$ , and  $H_2O$  were taken. The concentrations of plasma-produced  $NO$  and  $NO_2$  did not change with the addition of  $CH_4$ . Therefore, the rise in ignition temperature with increased  $CH_4$  addition to the oxidizer was not caused by the change of  $NO_x$ . The FT-IR measurements did show that a significant portion of the  $CH_4$  was oxidized to  $CO$ ,  $CO_2$ , and  $H_2O$ . Unfortunately, the inhibition of ignition due to the presence of  $CO_2$  was found to be minimal, on the order of a few Kelvin. The presence of  $H_2O$  only would increase the ignition temperature approximately a few Kelvin per 1 percent  $H_2O$  addition, which alone would not account for the up to 20 K rise of ignition temperatures that were observed. Furthermore, the concentrations of  $CO$  also would not change the ignition temperatures enough to match what was found experimentally; therefore, the unoxidized  $CH_4$  had to account for the changes in the ignition temperature.

Computational simulations were performed first with the concentrations of  $CH_4$ ,  $CO$ ,  $CO_2$ ,  $NO$ ,  $NO_2$  and  $H_2O$  measured by the FT-IR spectrometer and then were compared to the results of only  $CH_4$ ,  $NO$ , and  $NO_2$  addition. With the exclusion of  $CO$ ,  $CO_2$ , and  $H_2O$ , the ignition temperatures changed only by a few Kelvin when compared to having all the species introduced. This result proved that ignition was very sensitive to the concentrations of  $CH_4$  present. Sensitivity analysis for the two cases of 0.5%  $CH_4$  and 1%  $CH_4$  are shown in Fig.8. Once again, the  $CH_4$  was responsible for consuming the active radicals of  $OH$  by reaction R5, with the additional reaction of



R8

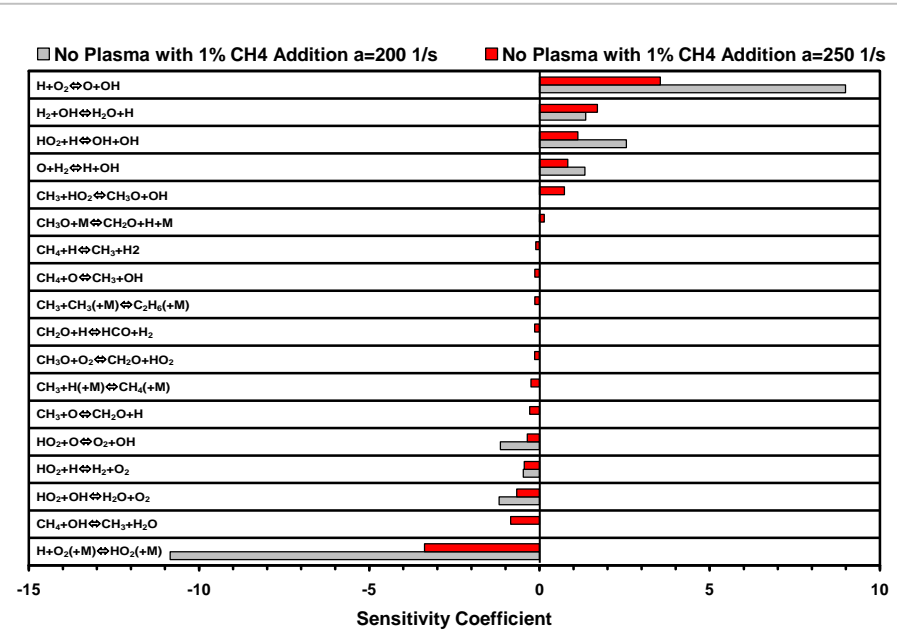


Fig.7 Sensitivity coefficients at ignition with and without MGA plasma activation of air and ultra-lean  $CH_4$  pre-mixtures as the oxidizer.

becoming important with increased CH<sub>4</sub> addition. For 0.2% CH<sub>4</sub> addition, none of the stable species measured by the FT-IR led to decreased ignition temperatures, hence more ignition enhancement. The under-prediction of ignition enhancement leaves open the possibility of the presence of other species that were not detected by the FT-IR that could enhance ignition further beyond what NO<sub>x</sub> did. The possibility of other stable species, such as H<sub>2</sub>, that cannot be measured because it does not absorb in the infrared, but more likely is the possibility of unstable or intermediate species that reached the reaction zone to enhance ignition, such as H, OH, O, etc., since small concentrations would yield significant results. Further investigation using different ultra-lean pre-mixtures with different concentrations of fuels would help to illuminate the possibility of these intermediate species leading to ignition enhancement.

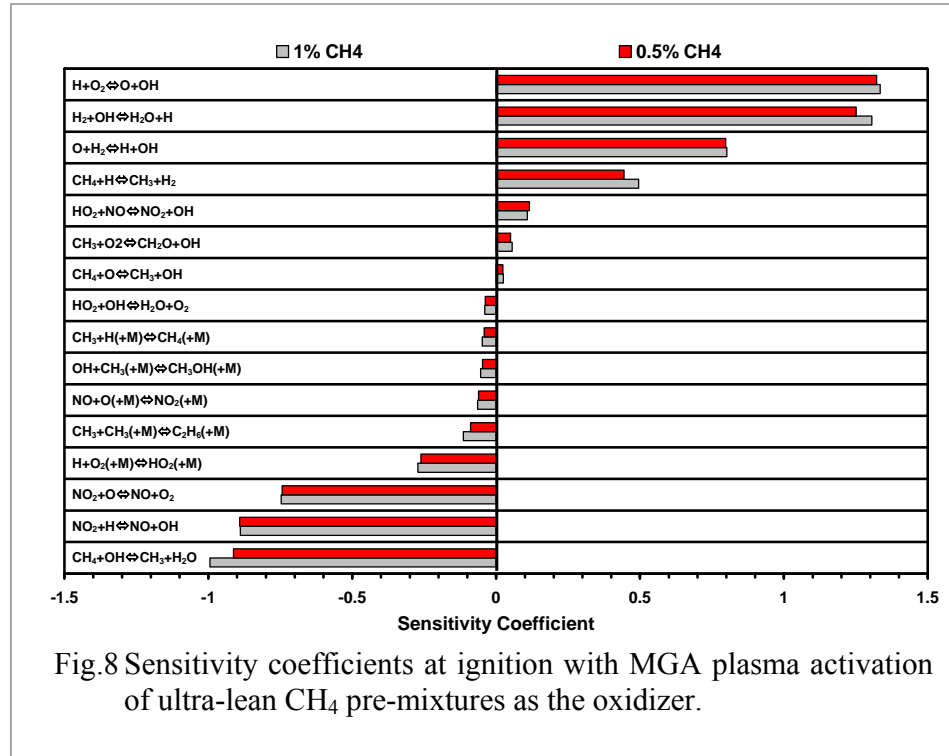


Fig.8 Sensitivity coefficients at ignition with MGA plasma activation of ultra-lean CH<sub>4</sub> pre-mixtures as the oxidizer.

#### 2.1.4. Conclusions

The present work isolated and identified the key non-thermal ignition mechanisms when using a non-equilibrium MGA plasma discharge of air, H<sub>2</sub>-air, and CH<sub>4</sub>-air ultra-lean pre-mixtures as the oxidizer of H<sub>2</sub> counterflow diffusion flames. Identification of the non-thermal ignition mechanisms came from comparisons of experimental measurements of ignition temperatures, FT-IR spectrometer measurements of stable plasma-produced species, and computational simulations, including sensitivity analysis to identify the key reactions and species at ignition. Without MGA activation of the oxidizer, the ultra-lean H<sub>2</sub> and CH<sub>4</sub> cases showed the inhibition of ignition by H<sub>2</sub>O and CH<sub>4</sub> by consuming active radicals. With MGA activation, there was a significant decrease in the ignition temperature, with NO<sub>x</sub> being the primary species causing enhancement when air was the oxidizer. With ultra-lean H<sub>2</sub>-air pre-mixtures as the oxidizer, no net change was observed in the ignition temperatures because of the NO<sub>x</sub> mitigating the effect of H<sub>2</sub>O by consuming the inactive HO<sub>2</sub> radical to produce active OH radicals. With MGA activation of the ultra-lean CH<sub>4</sub> pre-mixtures, the ignition temperatures increased significantly. The primary species that inhibited ignition was unoxidized CH<sub>4</sub>, with the ignition temperature being extremely sensitive to the concentration of CH<sub>4</sub>. Furthermore, the decreased



ignition temperatures for 0.2% CH<sub>4</sub> addition opens up the possibility of the presence of radicals or intermediate species that enhanced ignition. Overall, the MGA was able to mitigate the inhibiting effects of CH<sub>4</sub> on the ignition process because of the significant oxidation of CH<sub>4</sub> to CO, CO<sub>2</sub>, and H<sub>2</sub>O for all strain rates, as well as the large concentrations of ignition enhancing NO<sub>x</sub> that was produced; therefore, to observe the maximum ignition enhancement of H<sub>2</sub> with the presence of CH<sub>4</sub>, a non-equilibrium plasma should produce large concentrations of NO<sub>x</sub> and oxidize as much of the CH<sub>4</sub> as possible because of the extreme sensitivity to its concentrations.

## 2.2 Flame Propagation Enhancement by Plasma Generated O<sub>3</sub>

### 2.2.1 Experimental System and Methods

A laminar lifted flame burner was adopted for the combustion platform and used at a pressure of 101.3 kPa for all experiments. A schematic of the platform is shown in **Fig. 9**. The lifted flame burner consisted of a central fuel jet with an inner diameter of 0.271 mm that was located in a 90 mm inner diameter fused silica (quartz) tube to contain the co-flow of oxidizer. The fuel nozzle was shaped aerodynamically to produce a uniform velocity profile at the exit. The large ratio of diameters between the oxidizer co-flow and the fuel jet (>100) was used to ensure accurate comparisons to similarity solutions of the flow field. To ensure that the co-flow was uniform, two stainless steel meshes coated with silica for chemical inertness were separated by 3 cm and were located between the oxidizer inlet of the burner and the fuel jet exit. The gases used in the experiments were C<sub>3</sub>H<sub>8</sub> for the fuel and ultra-high purity O<sub>2</sub> (99.99%) and N<sub>2</sub> (99.95%) mixed for the oxidizer. The flow rate of the fuel was controlled with a calibrated mass flow meter, while the O<sub>2</sub> and N<sub>2</sub> were controlled with calibrated sonic nozzles. The undiluted ultra-high purity O<sub>2</sub> was passed through a dielectric barrier discharge device and then was merged with the N<sub>2</sub> stream to be introduced to the lifted flame burner. This configuration minimized any problems of NO<sub>x</sub> being produced in the discharge that would contaminate the flow. The dielectric barrier discharge device was comprised of a 110 mm long and 18 mm diameter co-axial sleeved tube geometry with a gap distance of 2 mm. The power was supplied by pulses of 3 kV to 10 kV positive and negative polarities with duration of 10 ns at FWHM with a frequency between 10 kHz and 40 kHz to produce different O<sub>3</sub> concentrations. Each pulse contained between 0.1 mJ and 1 mJ, providing between 1 W to 40 W total power. The discharge produced multiple oxygen-containing species, including O, O<sub>3</sub>, O<sub>2</sub>(v), O(<sup>1</sup>D), O(<sup>1</sup>S), O<sub>2</sub>(a<sup>1</sup>Δ<sub>g</sub>), O<sub>2</sub>(b<sup>1</sup>Σ<sub>g</sub>), etc.. To ensure that O<sub>3</sub> was the only species present in the flow when merged with the N<sub>2</sub> stream, a sufficient residence time

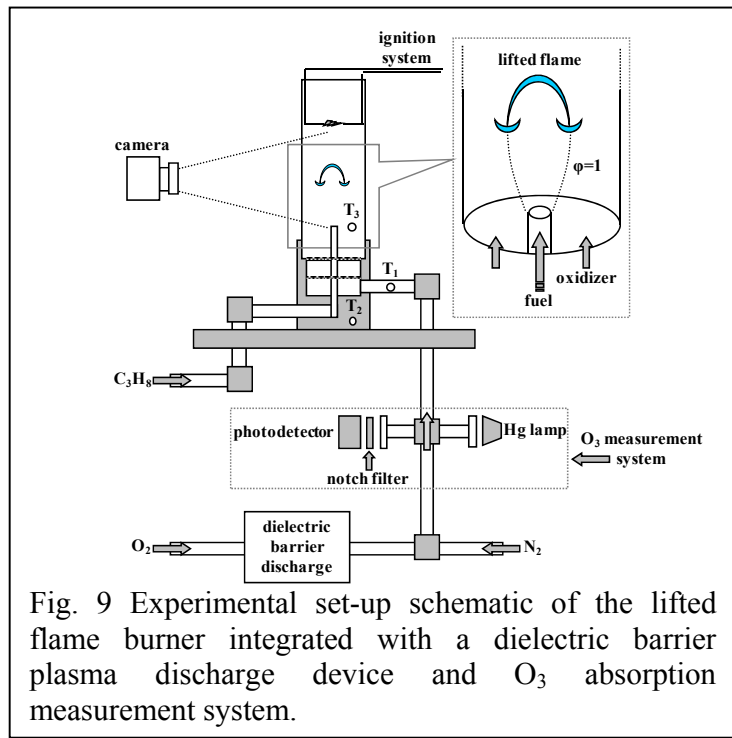


Fig. 9 Experimental set-up schematic of the lifted flame burner integrated with a dielectric barrier plasma discharge device and O<sub>3</sub> absorption measurement system.

was given to quench all plasma-produced species other than  $O_3$ . For example, **Table 1** lists the quenching rates of some of the common plasma-produced oxygen species. The atomic oxygen rapidly recombines with  $O_2$  to produce  $O_3$ , which is stable. The next longest lived species is  $O_2(a^1\Delta_g)$ , which is metastable, and at 101.3 kPa and 300 K has a collisional lifetime of approximately 20 milliseconds. With the flow rate and length of the tube between the dielectric barrier discharge and the merging with  $N_2$ , the residence time was over 100 milliseconds; therefore, when the dielectric barrier discharge was supplied with power, the only change in the gases entering the combustion system would be the addition of  $O_3$ .

Reaction	Reaction Constant [ $cm^3/molecule/s$ ]
$O+O_2+M \rightarrow O_3+M$	$6.0 \times 10^{-34} = (\text{HP limit } 3.61 \times 10^{-10})$
$O(^1D)+O_2 \rightarrow O+O_2$	$4.0 \times 10^{-11}$
$O_2(v)+O_2 \rightarrow O_2+O_2$	$1.73 \times 10^{-13}$
$O_2(b^1\Sigma_g)+O_2 \rightarrow O_2+O_2$	$4.1 \times 10^{-17}$
$O_2(a^1\Delta_g)+O_2 \rightarrow O_2+O_2$	$1.6 \times 10^{-18}$
$O_2(a^1\Delta_g)+Ar \rightarrow O_2+Ar$	$1.0 \times 10^{-20}$

Table 1 Reaction rates of plasma-produced oxygen species at 298 K. The term “HP” refers to the high pressure limit.

The high velocity fuel jet (3.5 – 10 m/s) and low velocity oxidizer co-flow (0.049 m/s) created a flow field with a stoichiometric contour where the premixed flame head of a lifted flame was located (shown in the top right insert in **Fig. 9**). The lifted flame, which also is called a tribrachial (triple) flame, had a premixed flame head anchored on the stoichiometric contour, followed by a diffusion flame tail. Direct photographs of the flame at various liftoff heights are shown in **Fig.10**. The lifted flame could be located at different stationary distances from the fuel jet nozzle depending upon the local flow velocity. For a fixed flow field, the flame was located in a stationary position where the lifted flame speed at the premixed flame head was balanced with the local flow velocity. If the flame speed increased, the liftoff height decreased to re-establish a local dynamic balance between the flame speed and flow velocity.

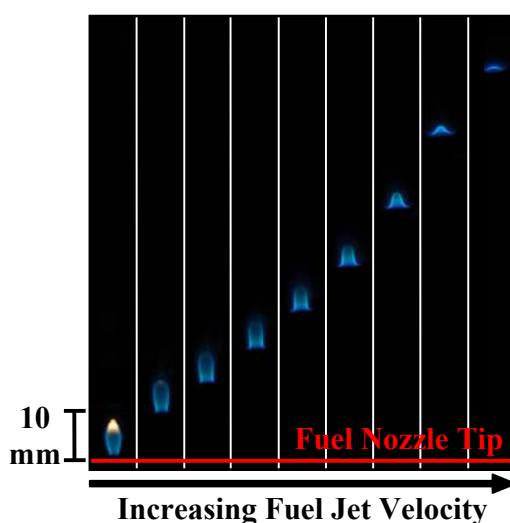


Fig. 10 Photographs of lifted flames at stationary positions for different fuel jet velocities.

A plot of the flame liftoff height versus fuel jet velocity is shown in **Fig. 11**. Due to the slow laminar boundary layer development and the velocity and concentration gradients created, the lifted flame height is very sensitive to the changes in flame speed and therefore provides excellent flame geometry for the direct observation of flame speed enhancement. For example, with only a small concentration of  $O_3$ , the flame liftoff height changes appreciably, as shown in **Fig. 11**. Since the fuel and oxidizer are not mixed far upstream of the flame, there is a very short residence time for the fuel and oxidizer to react in the cold flow. The short residence time helps to decouple the enhancement effects further, to be directly from reactions in the flame zone and not far upstream in the cold unreacted flow.

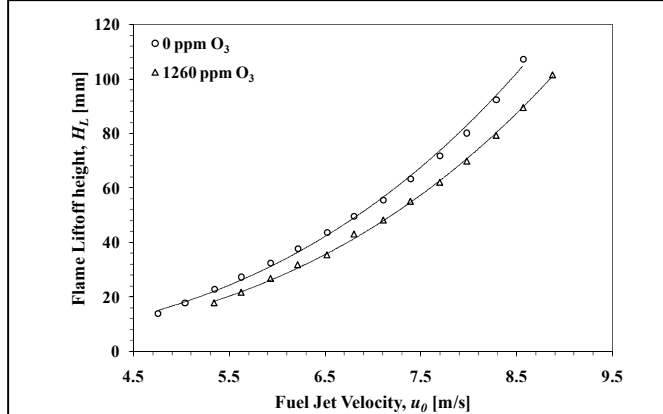


Fig. 11 Measurements of the flame liftoff height as a function of fuel jet velocity showing different flame stabilization locations from **Fig. 10**, as well as the sensitivity of flame speed changes.

Multiple temperatures were monitored by thermocouples placed on flow surfaces and in the flow and were recorded in the system. Temperatures were measured at points  $T_1$ ,  $T_2$ , and  $T_3$ , shown in **Fig. 9**, and were, respectively, the burner inlet tube surface temperature, burner surface temperature, and co-flow gas temperature. Throughout the experiments, the temperatures remained constant within 0.2 K between the plasma being turned on and off.

### 2.2.2 Quantitative Absorption Measurements of $O_3$

The  $O_3$  produced by the dielectric barrier discharge was measured using a one-pass, line-of-sight absorption cell in the flow downstream where the  $O_2$  and  $N_2$  streams merged. The absorption cell was comprised of a stainless steel compression cross fitting, with the side arms made of quartz tubes capped with UV quality windows. The cell was placed in the flow between the merging of the  $O_2$  and  $N_2$  streams and the burner. At one window, a mercury light with stable output provided ultraviolet light at the wavelength of 253.7 nm, where  $O_3$  has a peak absorption cross section of  $1.137 \times 10^{-17} \text{ cm}^2$  (at 300 K) in the Hartley band [51]. A 10 nm notch filter (isolating only the 253.7 nm mercury line) and a photodiode detector were placed at the exit of the transmission cell. No other species present in the flow ( $O_2$  and  $N_2$ ) absorb at this wavelength; therefore, the change in the transmittance of the cell with the plasma on and off could be used to determine the  $O_3$  concentration through the Beer-Lambert law

$$N_{\text{ozone}} = \frac{-\ln\left(\frac{I}{I_0}\right)}{\sigma_{\text{ozone}} L} \quad (3)$$

where  $N_{\text{ozone}}$  is the absolute number density of the absorbing species,  $O_3$ ,  $I$  the intensity of light with the presence of  $O_3$ ,  $I_0$  the intensity of light without the presence of  $O_3$ ,  $\sigma_{\text{ozone}}$  the absorption cross section of  $O_3$  at the excitation wavelength of 253.7 nm, and  $L$  the path length in the absorption cell (12.48 cm). The concentration then was calculated in parts per million (ppm) of  $O_3$  with an uncertainty of approximately  $\pm 2\%$  and a minimum detectable threshold of

approximately 15 ppm. The uncertainty and minimum detectable threshold came from the fluctuations in the intensity of the mercury light as a function of time during the experiments.

The O<sub>2</sub> loading was fixed at 18% O<sub>2</sub> in 82% N<sub>2</sub> for the oxidizer co-flow. This O<sub>2</sub> loading was chosen to ensure that the flame was completely within the laminar flow regime for the 0.271 mm diameter fuel nozzle used [52], as well as to maintain a maximum liftoff height well below the location of the igniter. The oxidizer co-flow velocity was fixed at 0.049 m/s, and the fuel velocity was small enough to have a nozzle-attached diffusion flame when ignited. The flame was photographed using a high resolution (10.2 megapixel) Nikon D40x camera. Then the dielectric barrier discharge was turned on, and a photograph was taken again of the stationary flame. The fuel velocity then was increased in small increments. At each increment photographs were taken of the flame with the dielectric barrier discharge off and on. This procedure was executed for at least ten flame liftoff heights between a nozzle-attached flame and a flame at the top of the stoichiometric contour. The experimental repeatability of flame liftoff height as a function of fuel jet velocity was tested carefully multiple times. The results showed that the lifted flame co-flow system had deviations in the flame liftoff height that were negligibly small at less than 1 mm.

For each condition where the dielectric barrier discharge was on, the O<sub>3</sub> concentration was measured in the absorption cell. To ensure that the O<sub>3</sub> measured in the absorption cell was the concentration that was present at the flame front, the experiments were performed with the absorption cell at different distances and flow residence times between the merging of the O<sub>2</sub> and N<sub>2</sub> and measuring location, as well as between the measuring location and the flame. There was no change in the O<sub>3</sub> concentration measured and/or a change in the flame enhancement by O<sub>3</sub>, confirming that the O<sub>3</sub> concentration measured in the absorption cell was the concentration present at the flame.

### 2.2.3. Results and Discussion

The lifted flame was established for fixed oxidizer co-flow velocity and O<sub>2</sub> loading (18% O<sub>2</sub> in 82% N<sub>2</sub>). The fuel jet velocity was increased, and pictures were taken at each stationary flame condition with and without O<sub>3</sub> present in the oxidizer (**Fig. 9**). More than ten fuel jet velocities were chosen to give a complete data range between a nozzle-attached flame and blowout of a lifted flame at the top of the stoichiometric contour. Since the fuel jet velocity was almost a factor of 100 larger than the co-flow velocity and the fuel jet diameter was more than 100 times smaller than the co-flow diameter, a similarity solution was applicable for the cold flow. The similarity solution was used to find where the stoichiometric contour existed and hence where the premixed head of the lifted flame was anchored.

By accounting for the density, the virtual origin, and co-flow velocity for uniform jet velocity profile at the nozzle exit, the local flow velocity,  $u$ , and fuel concentration,  $Y_F$ , can be derived in terms of the non-dimensional axial distance,  $X$ , and radius,  $R$ , from the similarity solution in the following equations, respectively.

$$\frac{u - V_{co}}{u_0 - V_{co}} = a \frac{\left(1 - \frac{q}{a}\right)}{1 - q} \frac{3}{32(X - X_v)} \frac{1}{\left[1 + 3a\left(1 - \frac{q}{a}\right)\left(\frac{R}{32(X + X_v)}\right)^2\right]^2} \quad (4)$$

$$Y_F = a(2Sc + 1) \frac{1}{32(X - X_{v,F})} \frac{1}{\left[ 1 + 3a \left( 1 - \frac{q}{a} \right) \left( \frac{R}{32(X + X_{v,F})} \right)^2 \right]^{2Sc}} \quad (5)$$

The non-dimensional axial distance and radius are defined as  $X = x/(dRe)$  and  $R = r/r_o$ , respectively, where  $x$  is the distance from the fuel nozzle tip,  $r$  the radial distance from the centerline,  $d$  and  $r_o$  the diameter and radius of the fuel nozzle, respectively,  $Re$  the Reynolds number defined as  $u_0 d / \nu_\infty$ ,  $u_0$  the initial jet velocity, and  $\nu_\infty$  the kinematic viscosity ( $1.574 \times 10^{-5} \text{ m}^2/\text{s}$  was used, which is for 18%  $\text{O}_2$  in 82%  $\text{N}_2$ ). Also,  $V_{co}$  is the co-flow velocity,  $a$  the density ratio between the fuel and oxidizer  $\rho_F/\rho_\infty$ ,  $q$  the ratio between the co-flow velocity and initial jet velocity  $V_{co}/u_0$ ,  $Sc$  the Schmidt number of  $\text{C}_3\text{H}_8$  ( $Sc = 1.366$ ) that was the fuel used in the experiments, and  $X_v$  and  $X_{v,F}$  the virtual origins for velocity and concentration of the fuel jet, respectively.

Using the similarity equation for velocity and concentration, the stoichiometric contour was found and compared with the flame location in the experiments. **Figure 12** shows a plot of the experimental results of flame radius normalized by the nozzle radius at various conditions of fuel jet velocity with and without the presence of  $\text{O}_3$  superimposed on a plot of the calculated cold flow stoichiometric contour. The good agreement between the flame radii with and without  $\text{O}_3$  addition and the cold flow stoichiometric contour shows that the similarity solution of the flow is representative of the flame location. Furthermore, by assuming a thin flame and neglecting the effect of thermal expansion, the local flow velocities along the stoichiometric contour can be considered comparable to the lifted flame speed. The approximation of a thin reaction zone has been validated

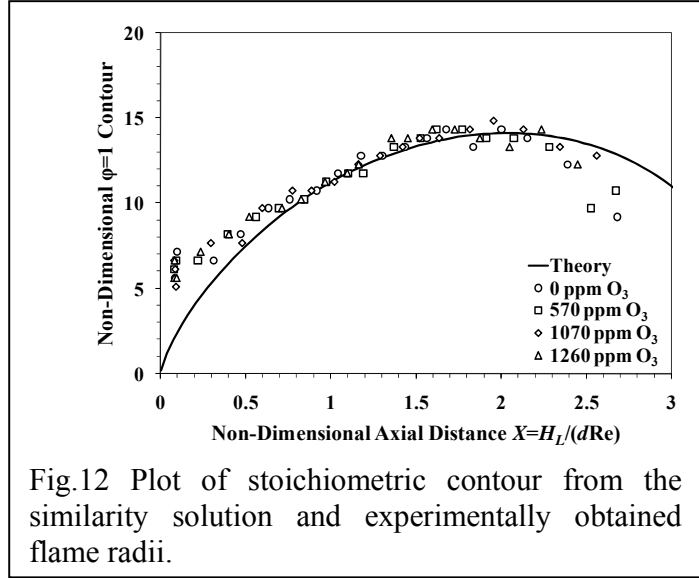
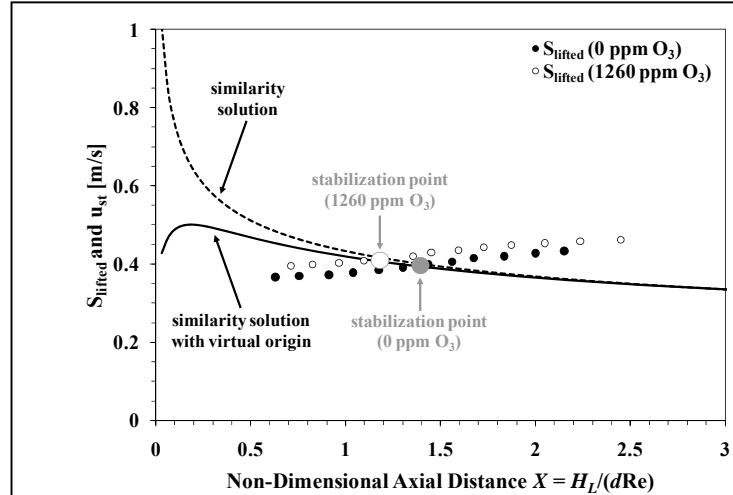


Fig.12 Plot of stoichiometric contour from the similarity solution and experimentally obtained flame radii.



**Fig. 13** Plot of the velocities along the stoichiometric contour found from similarity solutions with and without virtual origins along with the lifted flame speed with and without  $\text{O}_3$  addition showing the flame stabilization mechanisms.

in previous experiments [53,54,55,56,57], by showing that the extrapolation of tribrachial flame speed to the zero mixture fraction gradient agrees well with the maximum propagation speed of tribrachial flames predicted theoretically.

To evaluate the enhancement with  $O_3$  addition, an understanding of the flame stabilization mechanism is required. The stabilization mechanism of laminar lifted flames can be explained based upon the dynamic balance between the local flow velocity and flame speed along the stoichiometric contour. The leading edge of the lifted flame base at the premixed flame head always is located on the stoichiometric contour as shown in **Fig. 12**. The spatial profiles of local flow velocity from similarity solutions with and without the virtual origins are plotted in terms of non-dimensional axial distance,  $X$ , in **Fig. 13**. The flow velocities along the stoichiometric contour with and without the virtual origins are shown to deviate significantly when close to the fuel jet nozzle. Nevertheless, for the range of liftoff height used in the experiments, the deviation between the two solutions is on the order of 1%. Also plotted in **Fig. 13** are the lifted flame speeds with and without  $O_3$  addition, which were converted from the measurements of lifted flame heights by varying the initial jet velocity. Normally, without  $O_3$  addition, the lifted flame stabilizes where the local flow velocity on the stoichiometric contour is balanced with the lifted flame speed. When  $O_3$  is added to the system, the flame propagation speed is enhanced, and the flame moves upstream to a new stabilization location where there is a dynamic balance. The result in **Fig. 13** indicates clearly that the lifted flame is stabilized by the balance between the local flow velocity and flame propagation speed with and without  $O_3$  addition.

The lifted flame speeds were evaluated based upon the axial local flow velocity from the similarity solution of the cold flow at the measured liftoff heights with initial jet velocities. The results are plotted in **Fig. 14** as a function of fuel mixture fraction gradient. There is an enhancement of the lifted flame speed with increasing  $O_3$  concentration. Interestingly, the enhancement of lifted flame speed increases with increasing fuel mixture fraction gradient for the same concentration of  $O_3$ . The observed enhancement can be explained reasonably with a coupling effect between kinetic enhancement and changes to the flame front curvature leading to a hydrodynamic enhancement by considering the unique characteristics of the triple flame structure of laminar lifted flames.

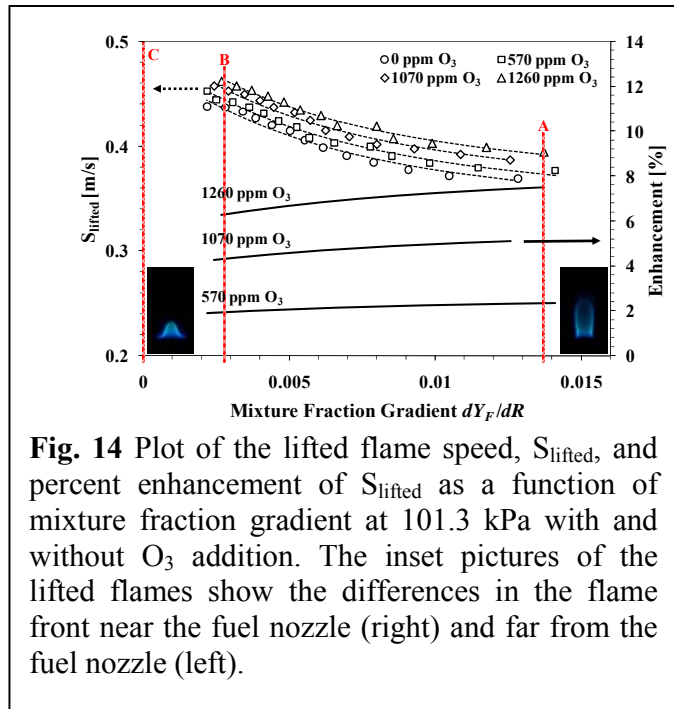


**Fig. 14** Plot of the lifted flame speed,  $S_{lifted}$ , and percent enhancement of  $S_{lifted}$  as a function of mixture fraction gradient at 101.3 kPa with and without  $O_3$  addition. The inset pictures of the lifted flames show the differences in the flame front near the fuel nozzle (right) and far from the fuel nozzle (left).

Firstly, numerical simulations were performed for equivalence ratios of 0.8 – 1.2 with and without 5000 ppm of  $O_3$ . This high concentration of  $O_3$ , which was larger than what was used in the experiments, was chosen in order to demonstrate more clearly what the effect was on the detailed structure of the flame that was not as easily observable numerically for lower  $O_3$  concentrations. The results in **Fig. 15** show that the laminar flame speed is enhanced more for lean and rich equivalence ratios than at stoichiometric conditions. This result is reasonable because lean and rich premixed flames have relatively weaker reactivity and lower chemical heat release compared to the stoichiometric condition; therefore, the off-stoichiometric flame is more sensitive to the same amount of energy input associated with the addition of  $O_3$ . The lifted flame speed is also a strong function of the curvature at the premixed flame front that is coupled not only with the fuel mixture fraction gradient but also with the flow velocity gradient, hence hydrodynamics. The premixed flame curvature of the triple flame structure is determined by the change of laminar flame speed with the equivalence ratio and the upstream flow profile based on the dynamic balance between flame speed and local flow velocity. With  $O_3$  addition to the co-flow of air, the non-uniform enhancement of laminar flame speed with the equivalence ratio induces an increase in the radius of the triple flame front since the lean and rich premixed flame will be enhanced more, as shown in **Fig. 15**. The larger radius of the flame leads to more significant flow redirection upstream of the flame; therefore, the local flow velocity at the premixed flame head will decrease and allow for enhanced lifted flame propagation speeds. Consequently, the lifted flame propagation speed is enhanced more by this effect because of the change in curvature of the flame front with  $O_3$  addition.

Secondly, the increase of enhancement with larger mixture fraction gradient can be attributed to the change of velocity gradient in the radial direction when the liftoff height is decreased by the addition of  $O_3$ . Previous work demonstrated experimentally that the triple flame structure of the lifted flame is tilted by the velocity gradient change and the tilting angle is increased proportionally with an increase of the velocity gradient. Thus, when the lifted flame moves to an upstream position because of flame speed enhancement from the addition of  $O_3$ , the lifted flame front is subjected to a larger velocity gradient, tilting the flame front further. The effect of the velocity gradient becomes more significant when the lifted flame is at a location closer to the nozzle because the velocity gradient also non-linearly increases with the decrease of the lifted flame height from the fuel jet exit. Consequently, the current evaluation method of lifted flame speed may over-predict the enhancement of lifted flame speed since the axial local flow velocity has been considered only.

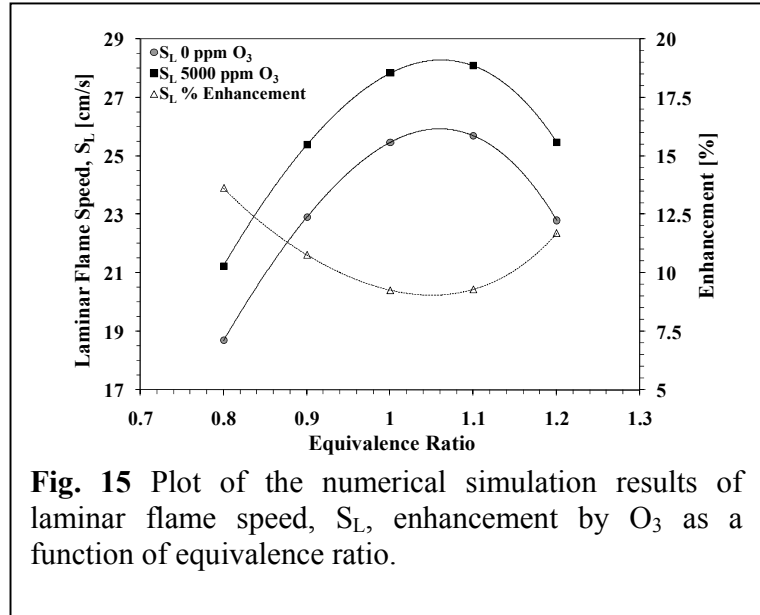


**Fig. 15** Plot of the numerical simulation results of laminar flame speed,  $S_L$ , enhancement by  $O_3$  as a function of equivalence ratio.

The detailed effects on flame front geometry changes through tilting, curvature, and stretch are out of the scope of the current study; however, the flame front geometry changes are extremely

important because of the increased flame propagation enhancement beyond the purely kinetic effect. This effect has been termed the kinetic-induced hydrodynamic enhancement.

To exclude the complicated enhancement mechanism caused by the hydrodynamic effects discussed above and to focus on the kinetic enhancement of the lifted flame speed, the variation of the lifted flame speed with fuel mixture fraction gradient was extrapolated to a zero mixture fraction gradient. The process allowed for direct comparison with the stoichiometric laminar flame speed. In the limit of zero mixture fraction gradient and flame curvature, the lifted flame speed,  $S_{lifted}$ , is related to the laminar flame speed,  $S_L$ , through the unburned to burned density ratio [58]

$$S_{lifted} \approx S_L \sqrt{\frac{\rho_{unburned}}{\rho_{burned}}};$$

therefore, the experimental results of lifted flame speed could be compared to calculated laminar flame speeds.

The enhancement of the local lifted flame speed and the extrapolated lifted flame speed are plotted as a function of  $O_3$  concentration in **Fig. 16** together with the numerical simulation results of purely kinetic enhancement. For the simulations with  $O_3$  addition, the O atoms were conserved in order not to perturb the total oxidizer fraction in the mixture. Furthermore, the  $O_3$  concentrations were adjusted to ppm concentrations for a stoichiometric flame instead of what was measured in the  $O_2$  and  $N_2$  mixture. For a large mixture fraction gradient, marked as *A* in **Fig. 14**, the enhancement is largest, as shown in **Fig. 16**. The factor-of-four difference in the flame speed enhancement between this fuel

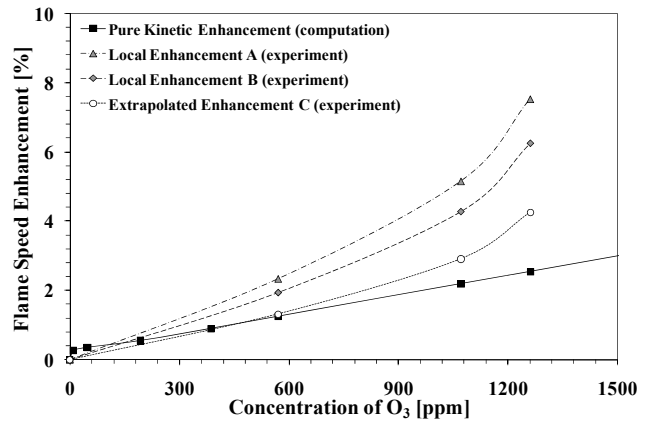


**Fig. 16** Plot of experimental results compared to numerical simulations. The local enhancement of “A” and “B” are indicated for large and small mixture fraction gradients, respectively, shown in **Fig. 13**, while “C” indicates the lifted flame speed enhancement when extrapolated to a zero mixture fraction gradient.

mixture fraction gradient and the purely kinetic enhancement are indicative of the kinetic-induced hydrodynamic enhancement described earlier in this section. For a small mixture fraction gradient, marked as *B* in **Fig. 14**, the local flame speed enhancement is lower, approaching the calculated purely kinetic enhancement results. The extrapolation to a zero mixture fraction gradient has been performed with a correlation factor  $R > 0.99$  and agreed well with numerical simulation results, marked as *C* in **Fig. 14**. The deviation between experimental and numerical results becomes slightly larger for larger  $O_3$  concentration. This effect once again is caused by the kinetic-induced hydrodynamic enhancement for larger concentrations of  $O_3$ . The smaller deviation between the extrapolated flame speed enhancement and the purely kinetic enhancement that was calculated is due to the extrapolation process averaging out the hydrodynamic enhancement. The details of the kinetic enhancement mechanism will be discussed in the following section with numerical simulation results.



To understand the flame speed enhancement pathways with O<sub>3</sub> addition, numerical simulations were performed using the PREMIX code from the CHEMKIN package [59]. The PREMIX code allows for one-dimensional calculations of laminar flames that can be used along with relation (5) to quantify the enhancement of lifted flame speed.

For the kinetic mechanism, the O<sub>3</sub> reactions [60,61] in **Table 2** were added to the C<sub>3</sub>H<sub>8</sub> mechanism [62]. The two most important reactions were the decomposition reaction of



and the O atom three body recombination reaction of



because of the production and consumption of O. The reaction of C<sub>3</sub>H<sub>8</sub> with O<sub>3</sub> also was added but was not significant in the reaction system. The low impact of this reaction was because the reaction rate was several orders of magnitude slower than the O<sub>3</sub> decomposition reaction [63]. The reaction is slow because O<sub>3</sub> does not react rapidly with saturated hydrocarbons. The adapted mechanism allowed for accurate predictions of the laminar flame speed, temperature, and species profiles for C<sub>3</sub>H<sub>8</sub> flames at a pressure of 101.3 kPa.

Reaction	Reaction Constant [cm <sup>3</sup> /mole/s]	Temperature Dependence	Activation Energy [kJ/mole]
O <sub>3</sub> +O <sub>2</sub> → O <sub>2</sub> +O+O <sub>2</sub>	1.54x10 <sup>14</sup>	0	96.5
O <sub>3</sub> +O → O <sub>2</sub> +O+O	2.48x10 <sup>15</sup>	0	95.09
O <sub>3</sub> +O <sub>3</sub> → O <sub>2</sub> +O+O <sub>3</sub>	4.40x10 <sup>14</sup>	0	96.5
O <sub>3</sub> +N <sub>2</sub> → O <sub>2</sub> +O+N <sub>2</sub>	4.00x10 <sup>14</sup>	0	94.84
O <sub>2</sub> +O+O <sub>2</sub> → O <sub>3</sub> +O <sub>2</sub>	3.26x10 <sup>19</sup>	-2.1	0
O <sub>2</sub> +O+N <sub>2</sub> → O <sub>3</sub> +N <sub>2</sub>	1.60x10 <sup>14</sup>	-0.4	-5.82
O <sub>2</sub> +O+O → O <sub>3</sub> +O	2.28x10 <sup>15</sup>	-0.5	-5.82
O <sub>2</sub> +O+O <sub>3</sub> → O <sub>3</sub> +O <sub>3</sub>	1.67x10 <sup>15</sup>	-0.5	-5.82
O <sub>2</sub> +O <sub>2</sub> → O+O+O <sub>2</sub>	9.80x10 <sup>24</sup>	-2.5	493.99
O <sub>2</sub> +O → O+O+O	3.50x10 <sup>25</sup>	-2.5	493.99
O <sub>2</sub> +O <sub>3</sub> → O+O+O <sub>3</sub>	1.20x10 <sup>19</sup>	-1	493.99
O <sub>2</sub> +H <sub>2</sub> O → O+O+H <sub>2</sub> O	1.20x10 <sup>19</sup>	-1	493.99
O+O+O <sub>2</sub> → O <sub>2</sub> +O <sub>2</sub>	1.50x10 <sup>16</sup>	-0.4	0
O+O+N <sub>2</sub> → O <sub>2</sub> +N <sub>2</sub>	6.00x10 <sup>13</sup>	0	-7.49
O+O+O → O <sub>2</sub> +O	5.34x10 <sup>16</sup>	-0.4	0
O+O+O <sub>3</sub> → O <sub>2</sub> +O <sub>3</sub>	1.30x10 <sup>14</sup>	0	-7.49
O <sub>2</sub> +O <sub>2</sub> → O <sub>3</sub> +O	1.20x10 <sup>13</sup>	0	420.12
O <sub>3</sub> +O → O <sub>2</sub> +O <sub>2</sub>	4.82x10 <sup>12</sup>	0	17.14
O <sub>3</sub> +H → O <sub>2</sub> +OH	6.87x10 <sup>13</sup>	0	3.64
O <sub>2</sub> +OH → H+O <sub>3</sub>	4.40x10 <sup>7</sup>	1.4	329.44
O <sub>3</sub> +OH → HO <sub>2</sub> +O <sub>2</sub>	9.60x10 <sup>11</sup>	0	8.32
O <sub>3</sub> +HO <sub>2</sub> → OH+O <sub>2</sub> +O <sub>2</sub>	1.66x10 <sup>11</sup>	-0.3	8.32

**Table 2** Rate constants for reactions of O<sub>3</sub> [60,61] that were added to the C<sub>3</sub>H<sub>8</sub> chemical mechanism [62].

When the temperature, O, and O<sub>3</sub> concentration profiles were plotted, it became apparent that there was an increase in the temperature early in the pre-heat zone and a shifting of the overall temperature gradient (Fig. 17). The early pre-heat zone of the flame shows that a decrease in the O<sub>3</sub> concentration corresponds to an increase in the O concentration and the temperature profile.

A rate of production analysis was performed to understand the underlying flux of species and the overall enhancement mechanism. In Fig. 17, the rate of production of O shows that, upon O<sub>3</sub> decomposition because of the slightly elevated temperatures in the pre-heat zone, O rapidly reacts with the fuel via the reactions



Reactions (8) and (9) provide the first key initiation steps in the extraction of chemical heat release by abstracting an H atom from the parent fuel to produce OH. Simultaneously, OH also is produced from the reaction of O<sub>3</sub> with H via



shown in Fig. 18. The rate constant for this reaction is given in Table 2. Reactions (8) – (10) are important because they provide the OH necessary to react and form H<sub>2</sub>O and thermal energy release to enhance the flame speed. A rate of production of OH analysis is shown in Fig. 18 and identifies the major reaction pathways that change significantly in the early stages of the flame following O<sub>3</sub> decomposition. The three most important reactions are



While reactions (11) – (13) all form H<sub>2</sub>O to produce heat release early in the flame, the two most important reactions are (11) and (12). The rate of heat release early in the pre-heat zone of the flame shows that reactions (11) and (12) are significant contributors of thermal energy, which elevates the temperature. Figure 19 shows increased chemical heat release at lower temperatures with O<sub>3</sub> addition, with the most significant impact between 700 K and 1300 K. The elevated levels of heat release earlier in the flame accelerate other reactions to change the structure of the flame, which, in turn, enhance the rate at which the flame can propagate. Furthermore, Fig. 19 shows that the peak heat release is higher with O<sub>3</sub> addition because of the additional energy that was coupled into the system by the plasma.

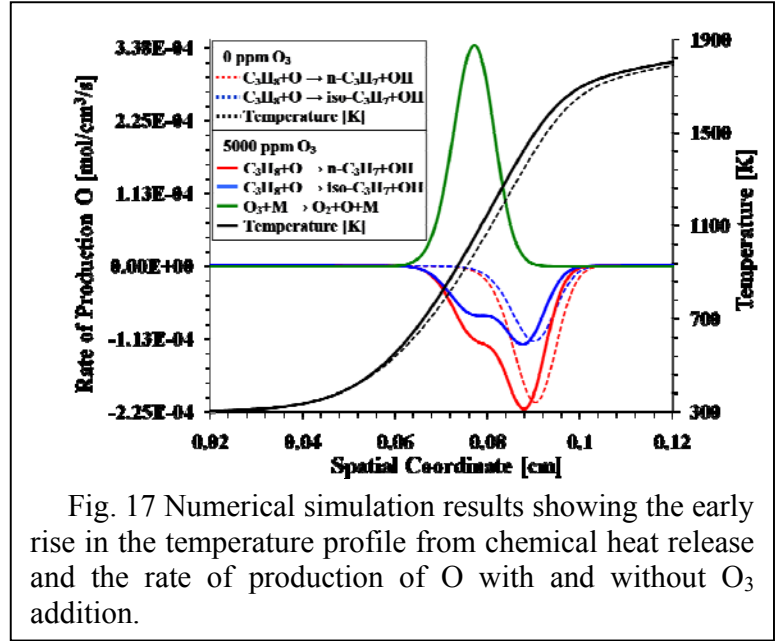
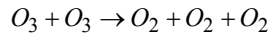


Fig. 17 Numerical simulation results showing the early rise in the temperature profile from chemical heat release and the rate of production of O with and without O<sub>3</sub> addition.

The enhancement scheme begins with the decomposition of  $O_3$  by reaction (6) early in the pre-heat zone of the flame, releasing O that rapidly reacts with the parent fuel via reactions (8) and (9). The OH that is produced then reacts to form  $H_2O$  and heat mostly via reactions (11) and (12) to elevate the temperatures. The elevated temperatures promote more rapid reactions early in the flame to enhance the flame propagation speed. The  $O_3$  acts as a transporter of energy from the plasma to the early stages of the flame in the pre-heat zone, where it seeds O into the flow to extract chemical heat release.

To demonstrate that the effect was not just simply the heat released after the decomposition of  $O_3$  and recombination of O, a fictitious reaction was added to the mechanism to quench the  $O_3$  to  $O_2$  to extract all of the energy to the flow far upstream of the flame zone. This comparison was accomplished by adding the reaction of



with a rate sufficiently fast to consume all of the  $O_3$  far upstream of the flame front, where the temperature was 300 K. The results of the flame speed enhancement with and without reaction (14) are shown in **Fig. 20** along with the experimental data. It is shown clearly that when  $O_3$  quenches far upstream of the flame, the temperature only increases by several degrees to enhance the flame speed much less than when  $O_3$  reaches the flame pre-heat zone; therefore, when  $O_3$  reaches the pre-heat zone of the flame, some chemical heat release is extracted to give significant flame speed enhancement. Furthermore, the results in **Fig. 20** also show good agreement between the enhancements found in the experiments and in the computations when the  $O_3$  reaches the pre-heat zone of the flame.

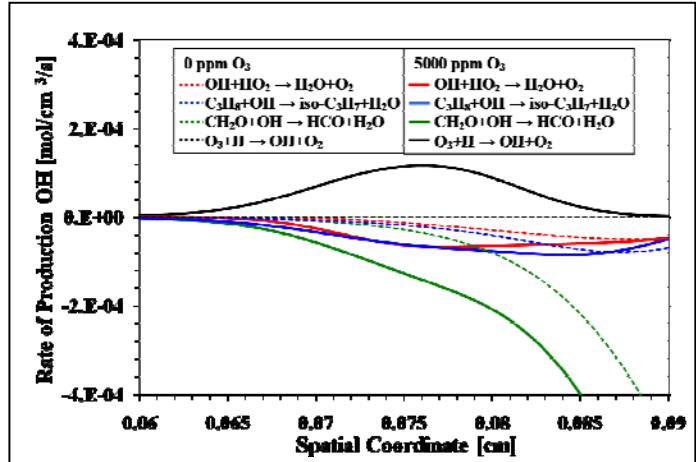


Fig.18 Fig. 11 Rate of production of OH showing change of reaction pathways with  $O_3$  addition to create stable products and heat release for flame speed enhancement.

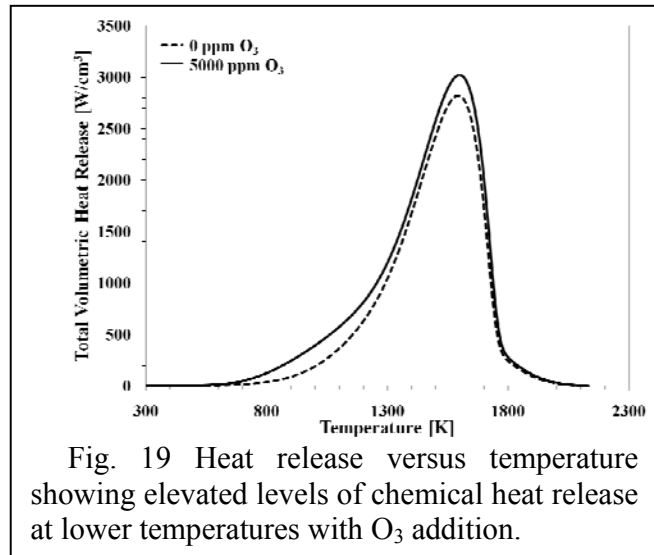


Fig. 19 Heat release versus temperature showing elevated levels of chemical heat release at lower temperatures with  $O_3$  addition.

With the knowledge that  $O_3$  addition to a lifted flame will enhance flame propagation speed significantly, it is of interest to take into account the efficiency of producing  $O_3$ . If one considers the production of  $O_3$  in a dielectric barrier, which is the most common production method, there exists a critical concentration at which the maximum flame speed enhancement is achieved. If large amounts of power are supplied to the discharge to

produce high concentrations of O, the recombination of O to  $O_2$  becomes a significant pathway, competing with the  $O_3$  production pathway of reaction (6). For example, if a concentration of 1% O is produced, every second O atom recombines to  $O_2$  instead of forming  $O_3$ . On the other hand, if the power of the discharge is too low, the energy loss to ions becomes increasingly important. A reasonable compromise is found when the dissociation in the plasma discharge reaches approximately 0.2%; therefore, with 0.2% (2000 ppm) of  $O_3$ , the kinetic enhancement of flame speed would be approximately 4%. With the addition of the changes in the flame front curvature caused by the kinetic enhancement, the overall flame speed would be enhanced between 10% and 15%; therefore, in a practical system, the production and injection of  $O_3$  in the cold transport to a flame can yield significant flame propagation enhancement with minimal energy expenditure.

#### 2.2.4. Conclusions

A platform to study quantitatively the enhancement effects of plasma-produced  $O_3$  on hydrocarbon flame speeds was developed.  $O_3$  had significant kinetic enhancement effects on the propagation speeds of  $C_3H_8$  lifted flames. Plasma-produced  $O_3$  becomes a carrier of O at low temperatures. Since the lifetime of O is extremely short, especially at room temperature because of recombination and wall quenching reactions, the attachment of O to  $O_2$  allows for extended cold transport of O. With temperatures lower than approximately 400 K, the  $O_3$  can transport O atoms almost indefinitely to a reaction system. The only difference in enhancement will come from the energy required to break the bond of the weakly attached O in  $O_3$ , which requires much less energy than producing O from  $O_2$ . Numerical simulation results showed that the O released upon  $O_3$  decomposition in the preheating- zone of the flame reacted rapidly with the fuel and atomic H to produce OH, which subsequently reacted with fuel and fuel fragments such as  $CH_2O$  to form  $H_2O$  and accelerated fuel oxidation. The chemical heat release early in the preheating zone of the flame resulted in increased propagation speed of the flame.

Equally important was the coupling effect that the kinetic enhancement had on the hydrodynamics at the flame front. The fuel and velocity gradients at the premixed flame head

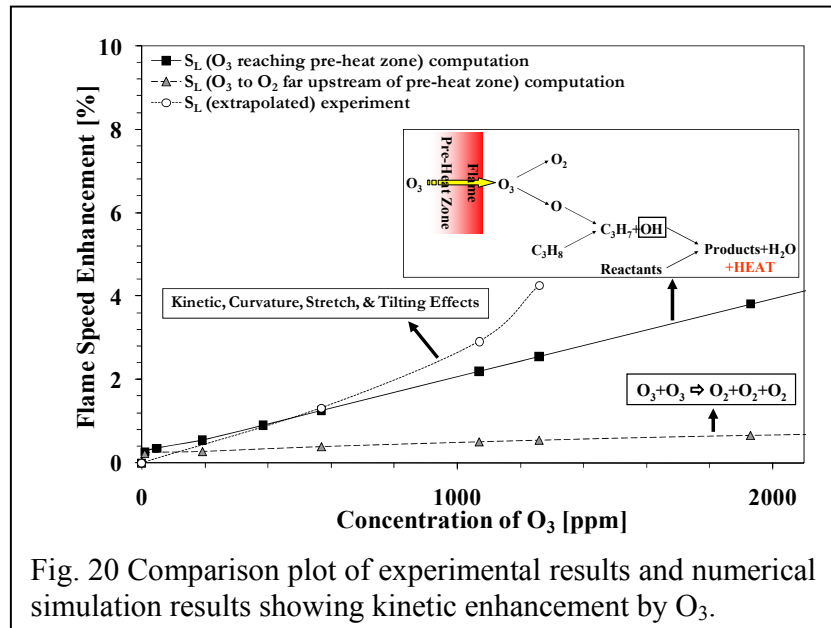


Fig. 20 Comparison plot of experimental results and numerical simulation results showing kinetic enhancement by  $O_3$ .

create a unique triple flame front with curvature, stretch, and tilting relative to the flow. Because of the unique triple flame structure of lifted flames, the presence of  $O_3$  at the flame front creates a kinetic enhancement that also induces hydrodynamic enhancement. The maximum overall flame speed enhancement in the laboratory coordinate was shown to be as high as 8% with 1260 ppm of  $O_3$ , while the enhancement locally was much lower at about 3%. When extrapolated to a zero mixture fraction gradient where the hydrodynamics of the flame were averaged and minimized, the enhancement was comparable to the pure kinetic enhancement at approximately 4%. The results indicate the very important finding that, in a practical system where there are fuel and velocity gradients, stretch, curvature, tilting, and significant concentrations of  $O_3$ , the flame speed can be enhanced greatly.

The results of the current research imply that, when energy is coupled into specific plasma-produced species, there is no requirement for the control of heat loss. For example, if energy is coupled into a reactive flow to raise the translational gas temperature only, there needs to be careful thermal management. When energy is coupled into stable species, no thermal management needs to be considered for  $O_3$  when the temperatures are below approximately 400 K. The energy contained within the species can be transported for significant distances and residence times and extracted at the combustion reaction zone.

Ozone addition illustrates the importance of timescales because, if  $O_3$  decomposes far upstream of the flame, the O released would recombine and not react with the fuel because the temperatures would not be high enough to support the propagation of those reactions within the flow residence time to the flame, but when the  $O_3$  decomposes and releases O to the reactants when the temperatures were only slightly elevated above the ambient, the fuel-plus-O reactions became dominant over recombination and quenching reactions. The chemical enthalpy that was extracted upstream of the flame stimulates other reactions, as well as the diffusion of heat, enhancing the propagation of the flame; therefore, the competition between the time scales of collisional quenching and reactive quenching is extremely critical when trying to achieve combustion enhancement through plasma activation.

Lastly, this work demonstrated another important step in developing an understanding of the most important plasma-produced species. With the knowledge of  $NO_x$  and  $O_3$ , less stable and shorter lifetime plasma-produced species now can be investigated more thoroughly. The results of  $O_3$  enhancement of flame propagation speed provided here gives a firm foundation, since  $O_3$  always will exist in an oxygen-containing plasma; therefore, the pursuit of shorter lifetime excited oxygen species, such as  $O_2(a^1\Delta_g)$ , can be pursued. The results of the effects of  $O_2(a^1\Delta_g)$  on flame propagation speed using a lifted flame apparatus at reduced pressures are discussed in the next section.

## **2.3 Flame Propagation Enhancement by Plasma Generated $O_2(a^1\Delta_g)$**

### ***2.3.1 Experimental System***

A laminar lifted flame burner in **Fig.21** was adopted for the combustion platform and was placed in a variable pressure chamber that could be used from atmospheric pressure down to 2.67 kPa with the installed vacuum and flow system. The lifted flame burner consisted of a central fuel jet with a diameter of 1.04 mm and was located in a 90 mm inner diameter fused silica (quartz) tube to contain the co-flow of  $O_2$  and Ar in the chamber. The gases used in the experiments were  $C_2H_4$  for the fuel and ultra-high purity  $O_2$  (99.99%) and Ar (99.95%) mixed for the oxidizer. The flow rate of the fuel was controlled with a calibrated mass flow meter,

while the  $O_2$  and Ar were controlled with calibrated sonic nozzles to give flow rate uncertainties of less than 1%.

To excite the co-flow in the low pressure experiments, an electrodeless microwave discharge (McCarroll cavity driven by an Ophos MPG-4M microwave power supply) with up to 100 Watts of power was used external to the chamber upstream of the lifted flame burner to activate the  $O_2$  in the mainly Ar flow (15%  $O_2$  in 85% Ar for 3.61 kPa and 11.9%  $O_2$  in 88.1% Ar for 6.73 kPa). The plasma was initiated in the microwave cavity by seeding the upstream flow with ionized gas created by a high-voltage, high-frequency Tesla coil. The mixture of ultra-high purity  $O_2$ /Ar was activated by the self-sustained microwave discharge that was maintained when the Tesla coil was switched off. The plasma system was chosen because of its flexibility of being used external to a quartz tube flow system, as well as its ease of tuning and stability for the range of pressures used in the experiments. Furthermore, the lower power output of the plasma system produced a glow discharge with a lower reduced electric field and an electron energy distribution function that was peaked at lower electron temperature where significant concentrations of  $O_2(a^1\Delta_g)$  could be excited from ground state  $O_2$ . Nevertheless, the microwave discharge produced excited Ar, as well as multiple oxygen-containing species, including  $O$ ,  $O_3$ ,  $O_2(v)$ ,  $O(^1D)$ ,  $O(^1S)$ ,  $O_2(a^1\Delta_g)$ ,  $O_2(b^1\Sigma_g)$ , etc.

The high-velocity fuel jet (approximately 20 m/s – 40 m/s) and low-velocity co-flow (approximately 0.15 m/s – 0.2 m/s) created a mixing layer with a stoichiometric contour where the premixed flame head of a lifted flame was located (shown in the top right insert in **Fig. 21**). The lifted flame, which is also called a tribrachial (triple) flame, had a premixed flame head and diffusion flame tail

where the flame always was anchored on the stoichiometric contour. The lifted flame could be located at different distances from the fuel jet nozzle depending upon the local flow velocity. For a fixed flow field, the flame was located in a stationary position, where the lifted flame speed at

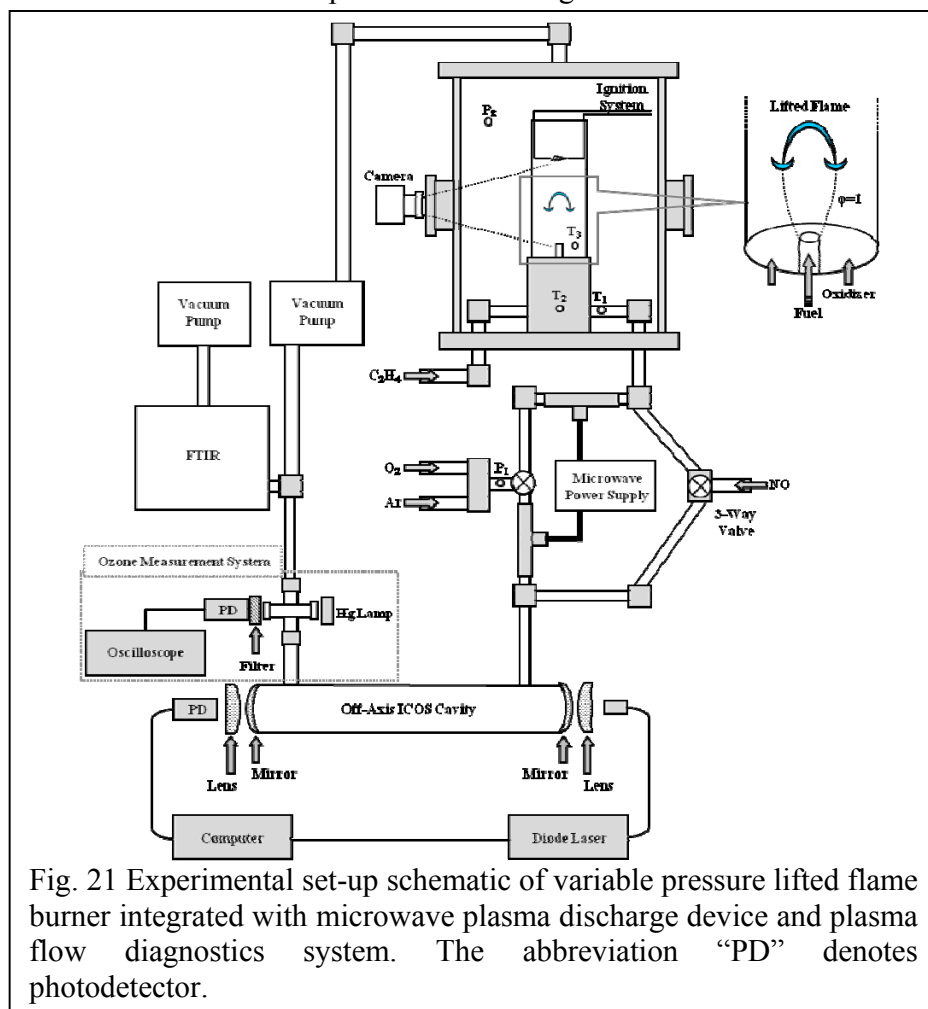


Fig. 21 Experimental set-up schematic of variable pressure lifted flame burner integrated with microwave plasma discharge device and plasma flow diagnostics system. The abbreviation “PD” denotes photodetector.

the premixed flame head was balanced with the local flow velocity. If the flame speed increased, the liftoff height decreased to re-establish a local dynamic balance between the flame speed and flow velocity.

Due to the slow laminar boundary layer development and the velocity and concentration gradients created, the lifted flame height was very sensitive to the changes in flame speed and therefore provided excellent flame geometry for the direct observation of flame speed enhancement. Since the fuel and oxidizer were not mixed far upstream of the flame, there was very short residence time for the fuel and oxidizer to react in the cold flow. The short residence time helped to decouple the enhancement effects further to be directly from reactions in the flame zone and not far upstream in the cold unreacted flow.

All surfaces with which the plasma afterglow gases came in contact were treated as chemically inert. The tubing used was fused silica (quartz), the fittings were 316 stainless steel (non-magnetic), and the lifted flame burner was coated with silica (Restek Silcosteel). The inert surfaces mitigated the quenching from active wall surfaces and promoted the transport of  $O_2(a^1\Delta_g)$  to the flame. Multiple temperatures and pressures were monitored and recorded in the system with thermocouples and pressure transducers, respectively. Temperatures were measured at points  $T_1$ ,  $T_2$ , and  $T_3$  shown in **Fig. 21**, corresponding to the burner inlet tube surface temperature, burner surface temperature, and co-flow gas temperature. Additionally, the pressure upstream of the microwave plasma and in the chamber, respectively at points  $P_1$  and  $P_2$  in **Fig. 21**, were monitored continuously and recorded.

The plasma-activated oxidizer flow was run through a series of diagnostics to quantify the concentrations of species produced by the plasma. The flow system used the same chemically inert flow surfaces and residence times for a direct comparison to the lifted flame system. The diagnostics were not run in situ with the flame system but instead as two separate systems with common flow control and plasma discharge. The systems were used separately because having the ICOS cavity between the plasma and flame would double the transport residence time and decrease the concentrations of the species of interest. For the 3.61 kPa and 6.73 kPa experiments, the residence times from the plasma to the end of the ICOS cavity were approximately 1320 milliseconds and 1680 milliseconds, respectively, and between the plasma and flame in the burner the times were approximately 910 milliseconds and 1470 milliseconds, respectively.

The  $O_2(a^1\Delta_g)$  produced by the microwave plasma discharge was measured by using highly sensitive integrated-cavity-output spectroscopy by absorption at the (1,0) band of the  $b^1\Sigma_g^+ - a^1\Delta_g$  Noxon system [64]. The ICOS system measured the average number density of  $O_2(a^1\Delta_g)$  across an 82.5 cm long (approximately 1500 millisecond residence time) absorption cell downstream of the plasma. The effective path length was greater than 78 kilometers due to multiple passes and

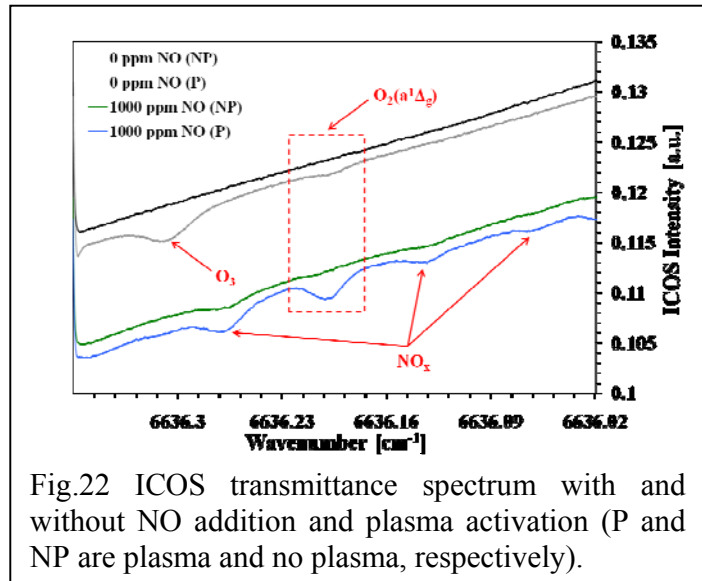


Fig.22 ICOS transmittance spectrum with and without NO addition and plasma activation (P and NP are plasma and no plasma, respectively).



provided accurate measurements down to  $10^{14}$  molecules/cm<sup>3</sup>. In **Fig. 22** the transmittance spectra from the ICOS cavity for the experimental conditions with and without NO addition and plasma activation are shown. The absorption feature demarcated by the red box shows the location of the Q(12) transition of O<sub>2</sub>(a<sup>1</sup>Δ<sub>g</sub>), which was the primary transition of interest [64]. The Q(12) transition was chosen for absorption measurements because there was no interference between it and any of the absorption features of other species present in the flow. In **Fig. 23** the measured absorption profile of O<sub>2</sub>(a<sup>1</sup>Δ<sub>g</sub>) using the Q(12) transition for plasma-activated Ar/O<sub>2</sub> at 3.61 kPa is shown. The fitted curve in **Fig. 23** was a function of the absorption pathlength and cross section, as well as broadening from pressure and temperature. A more detailed description of the measurement and curve fitting process to obtain absolute number densities of O<sub>2</sub>(a<sup>1</sup>Δ<sub>g</sub>) can be found in previous work [64].

The isolation of O<sub>2</sub>(a<sup>1</sup>Δ<sub>g</sub>) in the plasma afterglow was achieved with the addition of a small concentration of NO to the flow. The details of this approach are described in previous section. Quantitative measurements of NO and NO<sub>2</sub> were required to confirm the presence of these species in the system. To accomplish these measurements the flow was split downstream of the O<sub>3</sub> absorption cell to allow sampling with Fourier transform infrared (FTIR) spectroscopy. The pressure and temperature were fixed at 2 kPa and 373 K, respectively, in the FTIR cell for all experimental measurements to maintain sufficient flow rates and sampling times. The absorption features of NO and NO<sub>2</sub> were chosen where there would be no chance of interference from changes in the background or other species.

To avoid the complications of plasma disturbances in the combustion system, the flow was activated far upstream of the lifted flame. With the flow rates used in the experiments, the average residence times between the plasma and the flame were approximately one second. The significantly long residence time was chosen in order to quench the plasma-produced species that were not of interest in the experiments. Since the focus of the current experiments was to isolate O<sub>2</sub>(a<sup>1</sup>Δ<sub>g</sub>), Ar was used as the inert instead of N<sub>2</sub>. Using Ar served two purposes. First, Ar has only electronic excitation requiring 11.6 eV for the first electronic level; therefore, when using the low-power microwave system, most of the energy then will be deposited into the O<sub>2</sub> to produce O, O<sub>3</sub>, O<sub>2</sub>(a<sup>1</sup>Δ<sub>g</sub>), O<sub>2</sub>(b<sup>1</sup>Σ<sub>g</sub>), and metastable O and Ar. Second, without N<sub>2</sub>, there would be no nitrogen-containing species produced, specifically NO or NO<sub>2</sub>, simplifying the chemistry in the plasma and in the post-plasma flow.

With the one second residence time, the only two species that have long enough lifetime to allow for measurement and introduction to a combustion system are O<sub>3</sub> and O<sub>2</sub>(a<sup>1</sup>Δ<sub>g</sub>). A list of the primary quenching reactions of the oxygen containing species is given in **Table 3** in order of decreasing reaction rate. Quenching reactions with O<sub>2</sub> dominate over the inert species present and are, therefore, the reactions listed for a comparison. Ozone is the most stable species, with O<sub>2</sub>(a<sup>1</sup>Δ<sub>g</sub>) also having a long lifetime. All other species are quenched many times faster.

Beyond the gas-phase kinetics, the wall quenching effects have to be considered. Many species can be transported significant distances with inert wall surfaces; therefore, coating all wall surfaces with quartz or using quartz tubes is essential to ensure minimal quenching. Some examples of the relative reaction probabilities of plasma-produced species with a wall surface of Pyrex (similar to quartz) are shown in **Table 4**. Having large surface to volume ratios in the flow will suppress the concentrations of all species except O<sub>3</sub> and O<sub>2</sub>(a<sup>1</sup>Δ<sub>g</sub>).



Reaction	Reaction Constant [cm <sup>3</sup> /molecule/s]
O+O <sub>2</sub> +M → O <sub>3</sub> +M	6.0x10 <sup>-34</sup> = (HP limit 3.61x10 <sup>-10</sup> )
O( <sup>1</sup> D)+O <sub>2</sub> → O+O <sub>2</sub>	4.0x10 <sup>-11</sup>
O <sub>2</sub> (v)+O <sub>2</sub> → O <sub>2</sub> +O <sub>2</sub>	1.73x10 <sup>-13</sup>
O <sub>2</sub> (b <sup>1</sup> Σ <sub>g</sub> )+O <sub>2</sub> → O <sub>2</sub> +O <sub>2</sub>	4.1x10 <sup>-17</sup>
O <sub>2</sub> (a <sup>1</sup> Δ <sub>g</sub> )+O <sub>2</sub> → O <sub>2</sub> +O <sub>2</sub>	1.6x10 <sup>-18</sup>
O <sub>2</sub> (a <sup>1</sup> Δ <sub>g</sub> )+Ar → O <sub>2</sub> +Ar	1.0x10 <sup>-20</sup>

**Table 3** Reaction rates of plasma-produced oxygen species at 298 K. The term “HP” refers to the high pressure limit.

Wall Reaction	Reaction Probability
O <sub>2</sub> (a <sup>1</sup> Δ <sub>g</sub> )+wall → O <sub>2</sub>	2x10 <sup>-5</sup>
O <sub>2</sub> (b <sup>1</sup> Σ <sub>g</sub> )+wall → O <sub>2</sub>	2x10 <sup>-2</sup>
O <sub>2</sub> (v)+wall → O <sub>2</sub>	0.2
O( <sup>1</sup> D)+wall → O( <sup>3</sup> P)	1.0
O( <sup>1</sup> S)+wall → O( <sup>3</sup> P)	1.0
O+wall → ½O <sub>2</sub>	2x10 <sup>-2</sup>
M <sup>+</sup> +wall → M	1.0

**Table 4** Wall quenching probabilities of plasma-produced species for a Pyrex surface.

There remained the need to isolate O<sub>3</sub> and O<sub>2</sub>(a<sup>1</sup>Δ<sub>g</sub>) to observe their individual effects. Ozone can be isolated by simply using higher pressures because the O<sub>2</sub>(a<sup>1</sup>Δ<sub>g</sub>) will be quenched collisionally to O<sub>2</sub>(X<sup>3</sup>Σ<sub>g</sub>). To isolate O<sub>2</sub>(a<sup>1</sup>Δ<sub>g</sub>), a different approach needs to be taken to remove O<sub>3</sub>. To mitigate the effect of O<sub>3</sub> and completely isolate the effect of O<sub>2</sub>(a<sup>1</sup>Δ<sub>g</sub>), NO was added to the flow downstream of the plasma in the flow diagnostics system, as well as the combustion system. The addition of NO in prescribed concentrations served two purposes. First, it catalytically removed O<sub>3</sub> from the system to isolate O<sub>2</sub>(a<sup>1</sup>Δ<sub>g</sub>), and second, NO addition in the concentrations in the experiments would not interfere with the effects of O<sub>2</sub>(a<sup>1</sup>Δ<sub>g</sub>).

The isolation of O<sub>2</sub>(a<sup>1</sup>Δ<sub>g</sub>) with NO addition relies upon the reaction of NO with O<sub>3</sub> via



Reaction (15) is over three-orders of magnitude faster than NO with O<sub>2</sub>(a<sup>1</sup>Δ<sub>g</sub>), as shown in **Table 5**. The subsequent reaction of NO<sub>2</sub> with O<sub>2</sub>(a<sup>1</sup>Δ<sub>g</sub>) is also slow in comparison to reaction (15). The major consumption pathway of NO<sub>2</sub> would be from the reaction with O atoms via



Since O and O<sub>3</sub> are present at the same location in the flow tube, i.e., O atoms are converted to O<sub>3</sub>, NO acts as a catalyst, and very little is needed to eliminate the O<sub>3</sub> fully. The individual effects of O<sub>2</sub>(a<sup>1</sup>Δ<sub>g</sub>) can be selected by the use of NO addition. Finally, the presence of NO also can be used to determine the presence of O atoms via the well known O atom titration reaction



The absence of the greenish-yellow color in the plasma afterglow is used to assure that all the O atoms are quenched and not present in the flow system.

Reaction	Reaction Constant (cm <sup>3</sup> /molecule/s)
$O_2(a^1\Delta_g) + NO \rightarrow O_2 + NO$	$4.48 \times 10^{-17}$ [45]
$O_2(a^1\Delta_g) + NO \rightarrow O + NO_2$	$4.88 \times 10^{-18}$ [42]
$O_2(a^1\Delta_g) + NO_2 \rightarrow O_2 + NO_2$	$5.00 \times 10^{-18}$ [42]
$O_3 + NO \rightarrow O_2 + NO_2$	$1.80 \times 10^{-14}$ [40]
$O_3 + NO_2 \rightarrow O_2 + O_2 + NO$	$1.00 \times 10^{-18}$ [46]

**Table 5** Reaction rates of  $O_2(a^1\Delta_g)$  and  $O_3$  with NO and  $NO_2$  at 298 K.

### 2.3.2 Results and Discussion

To investigate the flame speed enhancement by  $O_2(a^1\Delta_g)$ , reduced pressures were used to suppress the quenching and recombination rates. The ICOS and  $O_3$  absorption diagnostics were used initially to measure  $O_2(a^1\Delta_g)$  and  $O_3$  as functions of pressure and  $O_2$  concentrations. The results in **Fig. 23** show that there remain significant concentrations of  $O_3$ , despite the decrease of the pressure. At lower pressure and  $O_2$  loading in Ar, the  $O_2(a^1\Delta_g)$  was in significantly greater concentration than  $O_3$ . Unfortunately, stable flames under lower pressure and  $O_2$  loadings were difficult to achieve; therefore, the removal of  $O_3$  was warranted for the isolated study of  $O_2(a^1\Delta_g)$ .

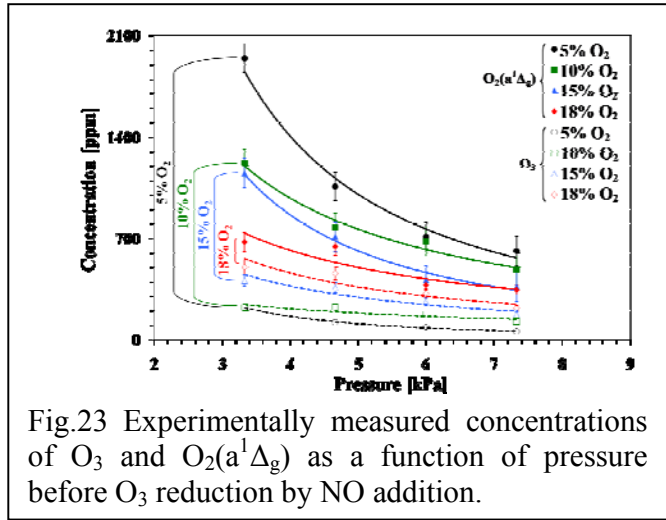


Fig.23 Experimentally measured concentrations of  $O_3$  and  $O_2(a^1\Delta_g)$  as a function of pressure before  $O_3$  reduction by NO addition.

The results in **Fig. 24** show that the addition of NO suppressed the concentration of  $O_3$  below the threshold that could be measured (ppm levels), while the  $O_2(a^1\Delta_g)$  concentration at a given residence time increased by almost an order of magnitude over a wide pressure range. Since the NO addition worked catalytically to reduce the  $O_2(a^1\Delta_g)$ -quenching species of  $O_3$  and O through reactions (15) and (16), the process was heavily reliant upon the concentration of O where the NO was added to the system. With the flow rates used in the system, the residence time between the plasma and the location of NO addition was approximately 5 ms.

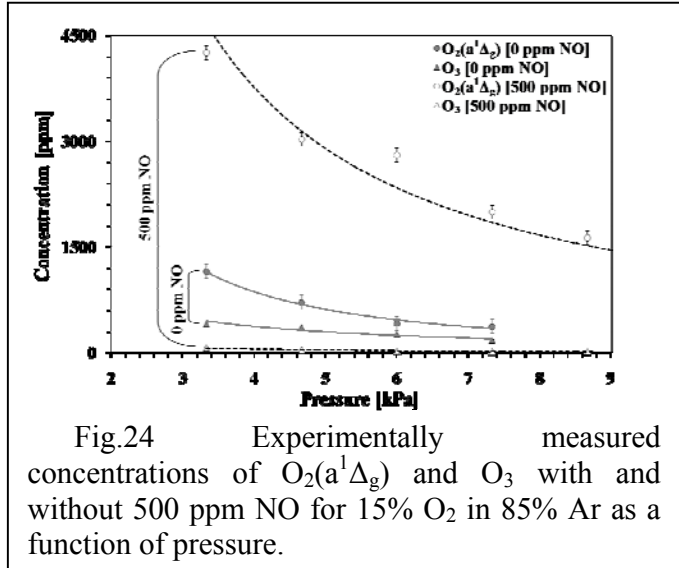


Fig.24 Experimentally measured concentrations of  $O_2(a^1\Delta_g)$  and  $O_3$  with and without 500 ppm NO for 15%  $O_2$  in 85% Ar as a function of pressure.

For the pressures used in the experiments, there was a significant concentration of O in relation to  $O_3$ ; nevertheless, the concentrations of NO and  $NO_2$  needed to be verified to ensure that the  $NO_2$  concentration remained negligible.

To confirm that there was no conversion of NO to NO<sub>2</sub>, measurements were taken using the FTIR with the plasma off and on. The measurements were taken initially of the plasma off, where the FTIR measured the exact concentration of NO that was being added to the system. When the plasma was turned on, the NO concentration did not change, as shown in **Fig. 25**. To confirm further that there was no NO<sub>2</sub> production, **Fig. 26** shows that the concentration of NO<sub>2</sub> remained below the detectability threshold of the FTIR. Two reference absorption spectra of 500 ppm and 4000 ppm NO<sub>2</sub> that were taken at the same pressures and temperatures are shown for comparison and to demonstrate that the three peaks present can be resolved. The results show clearly that the highest concentration of NO<sub>2</sub> was on the order of 10's of ppm. Since flame speed enhancement by NO<sub>2</sub> is more than a factor of three smaller than the effect of O<sub>3</sub> for the same concentrations, the small concentration of NO<sub>2</sub> would have a negligible effect on flame speed. When NO was added to the plasma afterglow, the only plasma-produced species to survive would be O<sub>2</sub>(a<sup>1</sup>Δ<sub>g</sub>), and the NO concentration would remain constant.

To confirm further the chemical kinetic processes involved in the post-discharge gases in the system, a simple flow kinetic model was compiled to include O, O<sub>3</sub>, O<sub>2</sub>(a<sup>1</sup>Δ<sub>g</sub>), N<sub>2</sub>, and Ar. Nitrogen was included in the model because the NO being injected into the system downstream of the plasma was accompanied by N<sub>2</sub>. The presence of N<sub>2</sub> did not affect any of the results because N<sub>2</sub> did not react with any of the other species present in the system. The most critical reaction would be with O<sub>2</sub>(a<sup>1</sup>Δ<sub>g</sub>), but the quenching rate is of the same order as the rate with Ar. One of the most important initial conditions for the numerical simulations was the concentration of atomic oxygen. To find what concentrations existed in the experiments, an NO<sub>2</sub> titration technique was adopted. NO<sub>2</sub> was added to the plasma afterglow at the same location of NO injection, approximately 5 ms downstream of the plasma. The NO<sub>2</sub> titration technique works by reaction (16) being five orders of magnitude faster than reaction (17); therefore, when NO<sub>2</sub> was injected after the plasma, the FTIR was used to sample the flow downstream and monitor the NO-versus-NO<sub>2</sub> concentration. The NO<sub>2</sub> was added continually until the FTIR showed the presence of NO<sub>2</sub> and no changes in

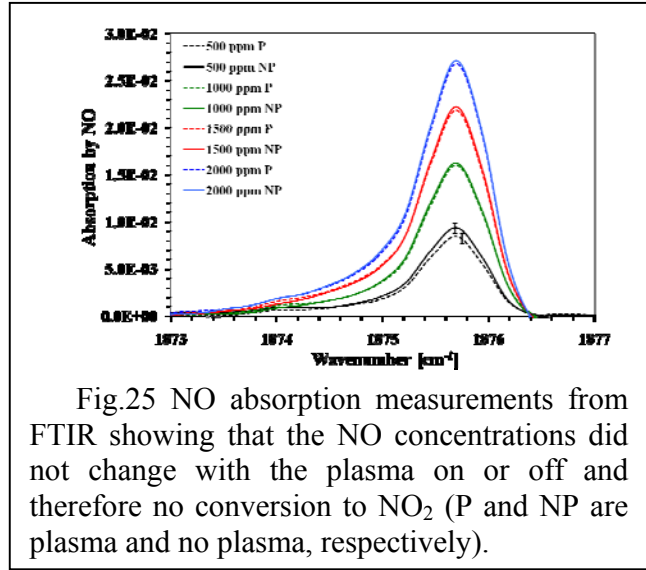


Fig.25 NO absorption measurements from FTIR showing that the NO concentrations did not change with the plasma on or off and therefore no conversion to NO<sub>2</sub> (P and NP are plasma and no plasma, respectively).

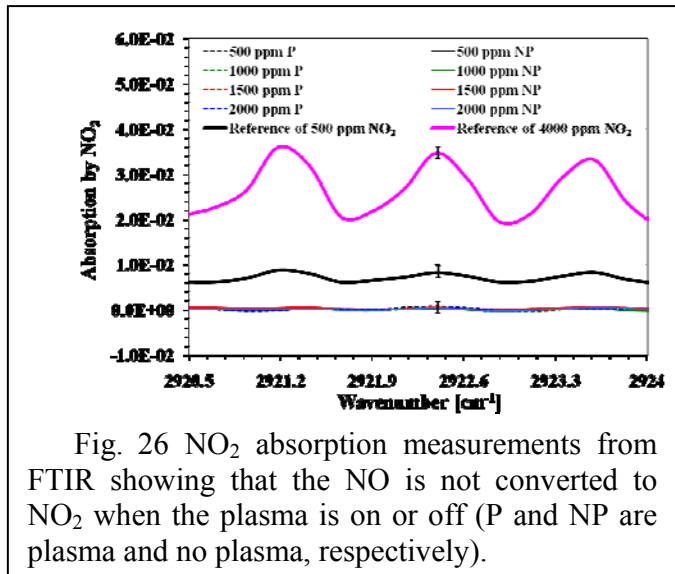


Fig. 26 NO<sub>2</sub> absorption measurements from FTIR showing that the NO is not converted to NO<sub>2</sub> when the plasma is on or off (P and NP are plasma and no plasma, respectively).

the concentration of NO. At that point, the concentration of NO<sub>2</sub> being added was equal to the concentration of O at the injection location in the flow. Furthermore, the lack of emission from reaction (17) also would indicate that O was no longer present in the flow. The NO<sub>2</sub> titration technique provided quantification of the O concentration within a 10% uncertainty to be used as an initial condition in the kinetic model.

Without NO addition to the plasma afterglow, the model predicted the concentrations of O<sub>3</sub> and O<sub>2</sub>(a<sup>1</sup>Δ<sub>g</sub>) well. With NO addition, if the simple flow kinetic model was maintained at 300 K, the catalytic cycle to remove O<sub>3</sub> was not complete and produced significant concentrations of NO<sub>2</sub>. Reaction (16) was not participating, possibly from the lack of presence of O. Realizing that the temperature of the gas in the plasma afterglow is not 300 K but starts at a temperature around 450 K and decreases to nearly room temperature after a short residence time,

the model was adjusted to account for this temperature condition. With a prescribed temperature gradient, the results with NO addition showed clearly that the catalytic cycle did not consume any NO and the NO<sub>2</sub> remained negligible (Fig. 27). Furthermore, the results without NO addition agreed well with the experiments (Fig. 27). The temperature gradient was critical to the catalytic cycle because of the quenching reactions of atomic oxygen. When the temperature was fixed at 300 K, the O atoms quenched quickly to produce O<sub>3</sub>, therefore not allowing the NO<sub>2</sub> to be converted back to NO. When the temperatures were higher at the beginning of the computation, the recombination reactions were suppressed, allowing for the catalytic cycle to be completed.

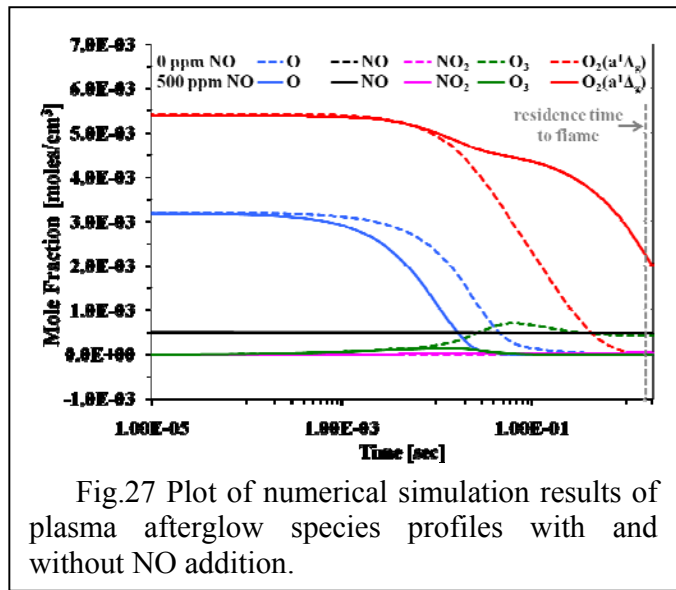


Fig.27 Plot of numerical simulation results of plasma afterglow species profiles with and without NO addition.

The validation of the simple flow model with the experimental results allowed for it to be used to find the concentrations of O<sub>2</sub>(a<sup>1</sup>Δ<sub>g</sub>) at the residence time of the flame in the burner system. The change of O<sub>2</sub>(a<sup>1</sup>Δ<sub>g</sub>) concentration at the residence time of the flame was very small, allowing for minimal error; therefore, the O<sub>2</sub>(a<sup>1</sup>Δ<sub>g</sub>) could be measured in the ICOS cavity and the kinetic model used to find the actual concentration at the specific flow residence time of the flame in the combustion system.

To examine the effects of O<sub>2</sub>(a<sup>1</sup>Δ<sub>g</sub>) on flame propagation speed, C<sub>2</sub>H<sub>4</sub> was used as the fuel to produce stable lifted flames at low pressures. The co-flow conditions of velocity and O<sub>2</sub> concentration in Ar were fixed, along with the fuel jet velocity, to establish a flame at a stationary lifted location. Photographs were taken of the flame while simultaneously recording the pressure and temperature. The microwave plasma then was turned on and photographs taken again of the flame with a lower liftoff height. The change in flame liftoff height was calculated from the photographs. A similar procedure was used again with NO addition just downstream of the microwave plasma cavity, replicating the residence times in the plasma afterglow diagnostics system. The results showed that there was a significant change in the flame liftoff height when the plasma was turned on with and without the addition of NO; therefore, the flame propagation enhancement came from a combination of O<sub>3</sub> and O<sub>2</sub>(a<sup>1</sup>Δ<sub>g</sub>) without NO addition and only from

$O_2(a^1\Delta_g)$  with NO addition. Concentrations between 500 ppm and 2000 ppm of NO were added downstream of the plasma to give different concentrations of  $O_2(a^1\Delta_g)$  at the flame front. The more NO that was added, the faster the  $O_3$  and O were quenched before they quenched  $O_2(a^1\Delta_g)$ .

The experiments were performed for several conditions at both 3.61 kPa and 6.73 kPa. The flow field, temperature, and pressure remained constant when the plasma was cycled off and on, so a direct comparison between plasma off and on conditions can be attributed to the enhancement by  $O_3$  and  $O_2(a^1\Delta_g)$ . The temperature and pressure remained constant within an uncertainty of 0.1 K and 26.7 Pa respectively. Experiments were performed to verify quantitatively that the uncertainty in temperature and pressure was not affecting the flame liftoff height enough to mask the enhancement by  $O_3$  and  $O_2(a^1\Delta_g)$  addition. For a temperature change of 0.1 K, the flame liftoff height changed by 0.07 mm, and for a pressure change of 26.7 Pa the flame liftoff height changed by 0.29 mm. For the change in flame liftoff height observed in the experiments with  $O_3$  and  $O_2(a^1\Delta_g)$  addition, which was on the order of 5 mm to 10 mm, the uncertainty was more than an order of magnitude smaller.

The presence of NO did affect the flame structure by changing the stoichiometric contour and flame speed slightly, but the comparison was between the plasma being off and on with constant NO addition. Since the flow diagnostics showed that the NO acted catalytically to reduce the  $O_3$  and did not change in concentration, the conditions of the plasma being off and on could be compared directly. The near-zero concentrations of  $NO_2$  would have a negligible effect on flame speed, since the enhancement was calculated to be more than three times lower than that of  $O_3$ .

$O_2(a^1\Delta_g)$ [ppm]	$O_3$ [ppm]	$\Delta H_L$ [mm]
215	513	7.15
3851	0	4.76
5416	0	7.31
5571	0	6.82
5596	0	6.83

**Table 6** Change in flame liftoff height ( $\Delta H_L$ ) with simulation corrected concentrations of  $O_2(a^1\Delta_g)$  and  $O_3$  present at flame for a plasma power of 80 Watts at 3.61 kPa.

$O_2(a^1\Delta_g)$ [ppm]	$O_3$ [ppm]	$\Delta H_L$ [mm]
10	423	7.70
2345	0	1.91
3285	0	5.64
3391	0	6.11

**Table 7** Change in flame liftoff height ( $\Delta H_L$ ) with simulation corrected concentrations of  $O_2(a^1\Delta_g)$  and  $O_3$  present at flame for a plasma power of 80 Watts at 6.73 kPa.

The same  $O_2$  loadings, flow rates, and pressures then were used on the plasma afterglow diagnostics system to find the concentrations of  $O_3$  and  $O_2(a^1\Delta_g)$  that were present at the lifted flame. The measured concentrations of  $O_3$  and  $O_2(a^1\Delta_g)$  were corrected for residence time using the kinetic model. The results are shown in **Table 6** and **Table 7** as a function of  $O_3$  and  $O_2(a^1\Delta_g)$  concentration for 3.61 kPa and 6.73 kPa, respectively. Overall, with NO addition, there was no change in the flow-field, temperature, or any species other than  $O_2(a^1\Delta_g)$  when the plasma was cycled on and off. Turning on the plasma was the equivalent of introducing a pure source of

$O_2(a^1\Delta_g)$ . The results in **Table 6** and **Table 7** show that there was a clear correlation between the concentration of  $O_2(a^1\Delta_g)$  present and the change in flame liftoff height. **Figure 28** shows the trend of increasing change in flame liftoff height, hence flame speed enhancement, with increasing  $O_2(a^1\Delta_g)$  concentration for both 3.61 kPa and 6.73 kPa. The experimental uncertainties for the change in flame liftoff height were  $\pm 0.5$  mm. For  $O_2(a^1\Delta_g)$ , the concentration uncertainty was  $\pm 500$  ppm, as shown by the error bars in **Fig. 28**.

With the results showing clearly the enhancement of flame propagation speed by  $O_2(a^1\Delta_g)$ , it was important to determine the enhancement quantitatively. Unlike the lifted flame at atmospheric pressure, a cold flow similarity solution does not describe the low-pressure experiments correctly; therefore, an indirect method was used to find the amount of flame speed enhancement quantitatively. The change in flame liftoff height shown in **Table 6**, **Table 7**, and **Fig. 28** indicates that approximately ten times the amount of  $O_2(a^1\Delta_g)$  (approximately 5500 ppm) was needed to achieve the same enhancement as  $O_3$  (approximately 500 ppm). Since the enhancement of

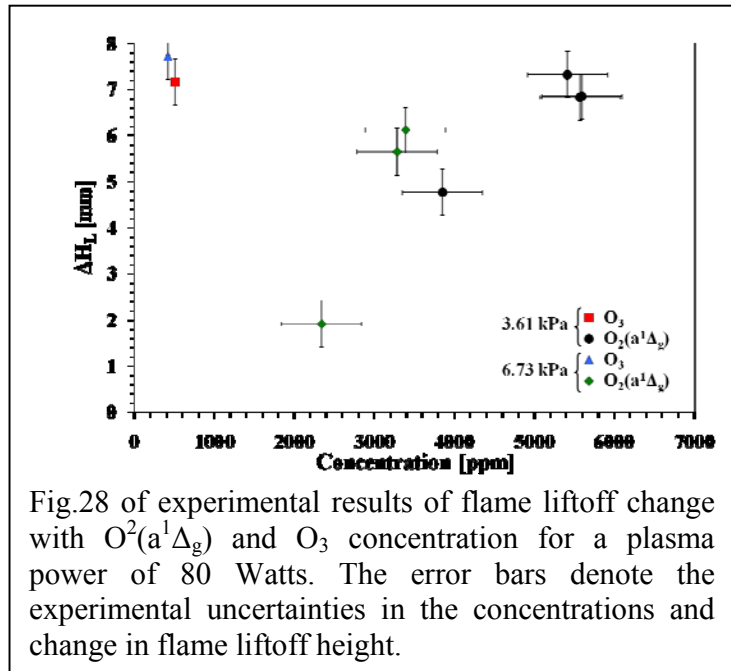


Fig.28 of experimental results of flame liftoff change with  $O_2(a^1\Delta_g)$  and  $O_3$  concentration for a plasma power of 80 Watts. The error bars denote the experimental uncertainties in the concentrations and change in flame liftoff height.

flame propagation speed was established with the addition of  $O_3$ , it can be used to quantify the enhancement by  $O_2(a^1\Delta_g)$ . The  $C_2H_4$  laminar and lifted flame speed enhancements were computed using the  $C_2H_4$  kinetic mechanisms [65] with the addition of the  $O_3$  reactions. The laminar and lifted flame speeds are related through the square root of the density ratio; therefore the, percent enhancements of the flame speeds were comparable. All of the experiments were performed for large flame liftoff heights where the mixture fraction gradient was small, and there was the closest agreement to the numerical simulations at a zero mixture fraction gradient. The lifted flame speed enhancement was used for comparison between experiments and numerical simulations. The results for the conditions of 500 ppm of  $O_3$  addition at 3.61 kPa and 6.73 kPa showed approximately 1% enhancement of the lifted flame speed (**Fig. 29**). Since the flame liftoff height change for 500 ppm  $O_3$  is equivalent to 5500 ppm  $O_2(a^1\Delta_g)$ , it was reasonable to assume that their effects on flame speed enhancement were comparable. The overall lifted flame speed enhancement would be higher because of the kinetic-induced hydrodynamic enhancement. If the effect of  $O_3$  at low pressure is comparable to what was found at high pressure, then 5500 ppm of  $O_2(a^1\Delta_g)$  will give approximately 2% to 3% enhancement of the lifted flame speed.

Reaction	Reaction Constant [cm <sup>3</sup> /molecule/s]	Temperature Dependence	Activation Energy [kJ/mole]
<b>Reactive Quenching of O<sub>2</sub>(a<sup>1</sup>Δ<sub>g</sub>)</b>			
H+O <sub>2</sub> → O+OH [50]	5.00x10 <sup>-9</sup>	0	60.3
H+O <sub>2</sub> (a <sup>1</sup> Δ <sub>g</sub> ) → O+OH [51]	1.82x10 <sup>-10</sup>	0	26.5
H+O <sub>2</sub> (a <sup>1</sup> Δ <sub>g</sub> ) → O+OH [29]	6.55x10 <sup>-11</sup>	0	21.0
OH+O <sub>2</sub> (a <sup>1</sup> Δ <sub>g</sub> ) → O+HO <sub>2</sub> [51]	2.16x10 <sup>-11</sup>	0	141.4
OH+O <sub>2</sub> (a <sup>1</sup> Δ <sub>g</sub> ) → H+O <sub>3</sub> [51]	7.31x10 <sup>-17</sup>	1.44	226.4
H <sub>2</sub> +O <sub>2</sub> (a <sup>1</sup> Δ <sub>g</sub> ) → OH+OH [51]	2.82x10 <sup>-9</sup>	0	141.4
H <sub>2</sub> +O <sub>2</sub> (a <sup>1</sup> Δ <sub>g</sub> ) → HO <sub>2</sub> +H [51]	4.13x10 <sup>-12</sup>	0	151.6
H <sub>2</sub> O+O <sub>2</sub> (a <sup>1</sup> Δ <sub>g</sub> ) → OH+HO <sub>2</sub> [27]	9.03x10 <sup>-8</sup>	0.5	209.7
H <sub>2</sub> O+O <sub>2</sub> (a <sup>1</sup> Δ <sub>g</sub> ) → O+H <sub>2</sub> O <sub>2</sub> [27]	2.05x10 <sup>-12</sup>	0.5	283.5
<b>Collisional Quenching of O<sub>2</sub>(a<sup>1</sup>Δ<sub>g</sub>)</b>			
H <sub>2</sub> +O <sub>2</sub> (a <sup>1</sup> Δ <sub>g</sub> ) → H <sub>2</sub> +O <sub>2</sub> [52]	2.16x10 <sup>-13</sup>	0	21.6
H <sub>2</sub> +O <sub>2</sub> (a <sup>1</sup> Δ <sub>g</sub> ) → H <sub>2</sub> +O <sub>2</sub> [29]	1.68x10 <sup>-12</sup>	0	32.0
H+O <sub>2</sub> (a <sup>1</sup> Δ <sub>g</sub> ) → H+O <sub>2</sub> [51]	6.97x10 <sup>-16</sup>	0	0
OH+O <sub>2</sub> (a <sup>1</sup> Δ <sub>g</sub> ) → OH+O <sub>2</sub> [51]	5.65x10 <sup>-18</sup>	0	0
HO <sub>2</sub> +O <sub>2</sub> (a <sup>1</sup> Δ <sub>g</sub> ) → HO <sub>2</sub> +O <sub>2</sub> [51]	5.65x10 <sup>-18</sup>	0	0
H <sub>2</sub> O+O <sub>2</sub> (a <sup>1</sup> Δ <sub>g</sub> ) → H <sub>2</sub> O+O <sub>2</sub> [51]	5.65x10 <sup>-18</sup>	0	0
H <sub>2</sub> O <sub>2</sub> +O <sub>2</sub> (a <sup>1</sup> Δ <sub>g</sub> ) → H <sub>2</sub> O <sub>2</sub> +O <sub>2</sub> [51]	5.65x10 <sup>-18</sup>	0	0
<b>Other Reactions with O<sub>2</sub>(a<sup>1</sup>Δ<sub>g</sub>)</b>			
H+HO <sub>2</sub> → H <sub>2</sub> +O <sub>2</sub> (a <sup>1</sup> Δ <sub>g</sub> ) [51]	3.32x10 <sup>-12</sup>	0	2.4
OH+O → H+O <sub>2</sub> (a <sup>1</sup> Δ <sub>g</sub> ) [51]	9.63x10 <sup>-12</sup>	0	51.8
O <sub>3</sub> +OH → HO <sub>2</sub> +O <sub>2</sub> (a <sup>1</sup> Δ <sub>g</sub> ) [51]	7.97x10 <sup>-13</sup>	0	8.3
O <sub>3</sub> +HO <sub>2</sub> → OH+O <sub>2</sub> +O <sub>2</sub> (a <sup>1</sup> Δ <sub>g</sub> ) [51]	1.66x10 <sup>-14</sup>	0	8.3
HO <sub>2</sub> +HO <sub>2</sub> → H <sub>2</sub> O <sub>2</sub> +O <sub>2</sub> (a <sup>1</sup> Δ <sub>g</sub> ) [51]	1.49x10 <sup>-11</sup>	0	4.2
H <sub>2</sub> O <sub>2</sub> +O → H <sub>2</sub> O+O <sub>2</sub> (a <sup>1</sup> Δ <sub>g</sub> ) [51]	6.97x10 <sup>-13</sup>	0	17.7

**Table 8** Reaction rates of O<sub>2</sub>(a<sup>1</sup>Δ<sub>g</sub>) with hydrogen containing species.

Numerical simulations were performed in order to explain the enhancement mechanism with the addition of O<sub>2</sub>(a<sup>1</sup>Δ<sub>g</sub>). The C<sub>2</sub>H<sub>4</sub> combustion mechanisms [65,66] with the O<sub>3</sub> reactions added were used along with the inclusion of O<sub>2</sub>(a<sup>1</sup>Δ<sub>g</sub>) reactions. The reactive and collisional quenching rates of O<sub>2</sub>(a<sup>1</sup>Δ<sub>g</sub>) with oxygen and inert species as functions of temperature have been well studied and were used to compute the cold flow transport of O<sub>2</sub>(a<sup>1</sup>Δ<sub>g</sub>) in the ICOS system and prior to the flame in the combustion system. These O<sub>2</sub>(a<sup>1</sup>Δ<sub>g</sub>) reactions were added to the C<sub>2</sub>H<sub>4</sub>/O<sub>3</sub> mechanisms. The reactions of O<sub>2</sub>(a<sup>1</sup>Δ<sub>g</sub>) with the fuel also have been well studied at 298 K, but there are little data at intermediate and high temperatures. The most studied O<sub>2</sub>(a<sup>1</sup>Δ<sub>g</sub>) reactions applicable to a combustion system are for H<sub>2</sub>-O<sub>2</sub> mixtures. These reactions of hydrogen and oxygen containing species with O<sub>2</sub>(a<sup>1</sup>Δ<sub>g</sub>) are shown in **Table 8** and have been compiled specifically for H<sub>2</sub>-O<sub>2</sub> mixtures activated by plasma. The rates were taken from previous numerical work on plasma-assisted H<sub>2</sub>-O<sub>2</sub> combustion systems, as well as from specific reaction rate studies [67,68,69]. A few differences arose, specifically regarding the two reactions





The reactions were added to the  $C_2H_4/O_3$  kinetic mechanisms and the results are shown in **Fig. 29** using the concentrations of  $O_3$  and  $O_2(a^1\Delta_g)$  from the experiments. The results of enhancement using the  $O_2(a^1\Delta_g)$  concentrations found in the experiments showed flame speed enhancement of more than 5%. When compared to the experimental results of lifted flame speed enhancement by  $O_3$  (that was found to be approximately 1%) there was a large discrepancy, which was well outside the uncertainties for the system. For example, in the experiments at 3.61 kPa, the change in flame liftoff height for 500 ppm  $O_3$  was approximately equal to 5500 ppm  $O_2(a^1\Delta_g)$  (**Fig. 28**). According to the numerical simulations, there was more than a factor of five difference in the enhancement of flame speed. Considering that the  $O_3$  and  $O_2(a^1\Delta_g)$  both should enhance the lifted flame speed similarly with the lean and rich enhancement more than for stoichiometric mixtures, there is a significant error in the  $O_2(a^1\Delta_g)$  kinetic calculations. With regard to the differences in the rates for reactions, the deviations in the flame speed enhancement were no more than  $\pm 4\%$ . The vertical error bars in **Fig. 29** show the negligible enhancement differences when using the two published rates for reactions, [18] and [19]; therefore, the sensitivity of the flame speed to the differences in reaction rates do not account for the significant deviations from the experiments.

To understand what caused the significant flame speed enhancement by  $O_2(a^1\Delta_g)$ , a rate of production plot of  $O_2(a^1\Delta_g)$  in the flame is shown in **Fig. 30**. The major consumption pathways of  $O_2(a^1\Delta_g)$  were from the branching reaction with H, with some contribution of collisional quenching by  $H_2$ . The reaction of  $O_2(a^1\Delta_g)$  with H will enhance the flame significantly, since it is a primary radical branching reaction. It was reasonable that the enhancement was so large in the numerical simulations.

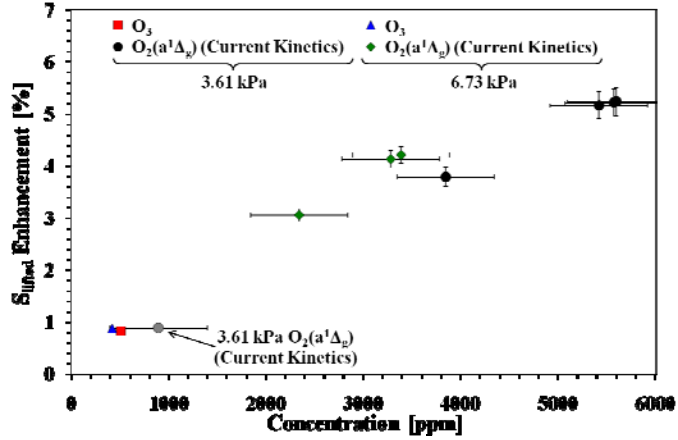


Fig.29 Plot of computational results of lifted flame speed enhancement with  $O_2(a^1\Delta_g)$  and  $O_3$ . The horizontal error bars denote the propagation of uncertainty from the concentrations found experimentally, while the vertical error bars denote the range of lifted flame speed enhancement when using the different published reaction rates.

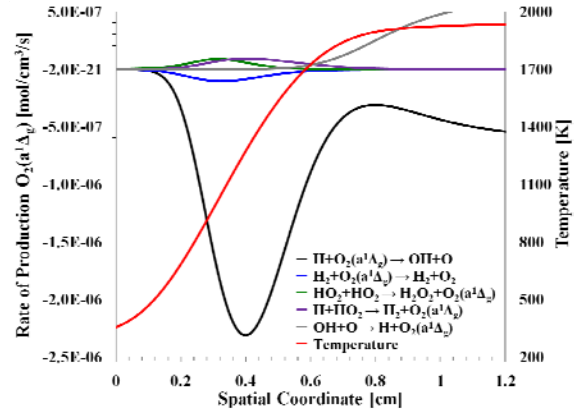


Fig.30 Rate of production plot of  $O_2(a^1\Delta_g)$  superimposed on the temperature profile showing the major consumption pathways of  $O_2(a^1\Delta_g)$  with current published rate data with hydrogen containing species.



The changes in the radical pool in the earlier stages of the flame are shown in **Fig. 31**. In the earlier stages of the flame where the temperature is elevated slightly between 400 K and 500 K, the  $O_2(a^1\Delta_g)$  begins to be consumed, causing a decrease in the  $C_2H_4$  concentration and a subsequent increase in O and OH. The increase in concentration of OH would provide chemical heat release through subsequent reactions earlier in the flame to enhance the overall flame speed significantly. The higher concentrations of OH in the earlier stages of the flame leading to chemical heat release and enhanced flame speed were shown through the study of  $O_3$  addition. The increase in the radical pool concentration of O from the reactions with  $O_2(a^1\Delta_g)$  were investigated in greater depth through a rate-of-production analysis. The results showed that the major pathway for O consumption was from the reaction with the parent fuel,  $C_2H_4$ , and its fragment,  $CH_3$ . The end results of flame propagation enhancement came from the increased radical pool concentration and extraction of chemical heat release earlier in the flame compared to the results with no  $O_2(a^1\Delta_g)$  addition. **Figure 32** clearly indicates the elevated levels of chemical heat release by showing the total volumetric heat release as a function of temperature in the flame. There is significantly more heat release between 800 K and 1500 K with  $O_2(a^1\Delta_g)$  addition, which aligns well with the peak consumption of  $O_2(a^1\Delta_g)$  and elevated radical concentrations, shown in **Fig. 30** and **Fig. 31**, respectively.

With an understanding of how  $O_2(a^1\Delta_g)$  enhanced the flame speed in the numerical simulations, it becomes apparent that there are two possible explanations for the discrepancy shown in **Fig. 29** with respect to the enhancement by  $O_3$  and  $O_2(a^1\Delta_g)$ . First, a significant concentration of the  $O_2(a^1\Delta_g)$  could quench before reacting with H. The collisional quenching reactions of  $O_2(a^1\Delta_g)$  with the parent fuel or its fragments could decrease the concentration significantly, thereby leading to less enhancement. To achieve the same enhancement of  $O_2(a^1\Delta_g)$  as the calculations with  $O_3$  indicate, approximately 900 ppm  $O_2(a^1\Delta_g)$  would be needed (shown in **Fig. 29** for 3.61 kPa). Approximately 4600 ppm of  $O_2(a^1\Delta_g)$  would have to quench

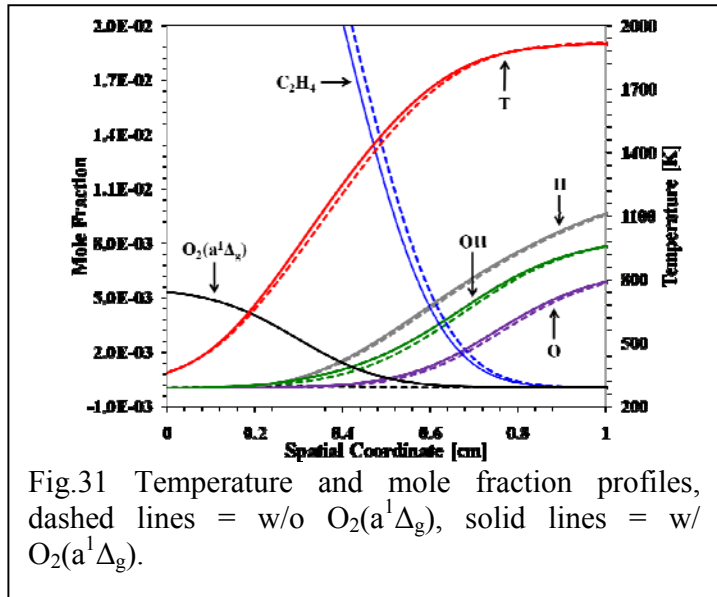


Fig.31 Temperature and mole fraction profiles, dashed lines = w/o  $O_2(a^1\Delta_g)$ , solid lines = w/  $O_2(a^1\Delta_g)$ .

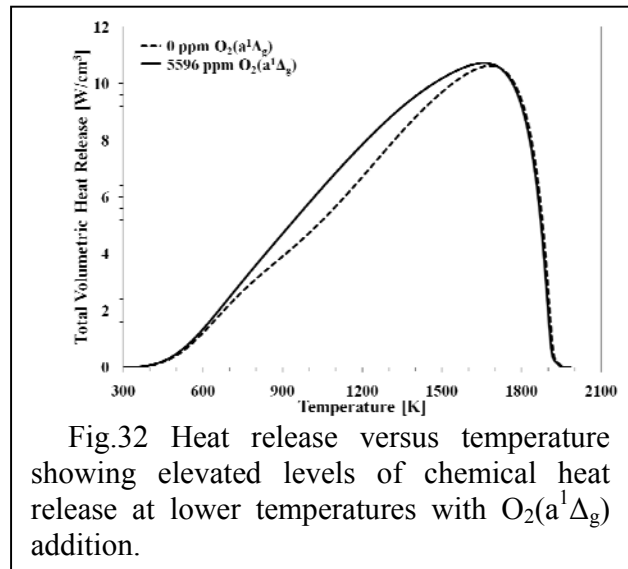


Fig.32 Heat release versus temperature showing elevated levels of chemical heat release at lower temperatures with  $O_2(a^1\Delta_g)$  addition.

collisionally, allowing only a small fraction of the original concentration to react with H. The enhancement would be less, especially if the dominating reactions of  $O_2(a^1\Delta_g)$  would be with the parent fuel and not providing chain branching as in the reaction of H with  $O_2(a^1\Delta_g)$ . Second, there could be a combination of reactive and collisional quenching pathways for  $O_2(a^1\Delta_g)$  that could be responsible for the enhancement observed in the experiments.

Reaction	Reaction Constant [cm <sup>3</sup> /molecule/s]	Temperature Dependence	Activation Energy [kJ]
$CH_4 + O_2(a^1\Delta_g) \rightarrow CH_4 + O_2$ [42]	$1.40 \times 10^{-18}$	0	0
$CH_4 + O_2(a^1\Delta_g) \rightarrow CH_3 + HO_2$ [54]	$6.14 \times 10^{-12}$	0	149.0
$C_2H_4 + O_2(a^1\Delta_g) \rightarrow C_2H_4 + O_2$ [*low]	$7.71 \times 10^{-16}$	0	15.0
$C_2H_4 + O_2(a^1\Delta_g) \rightarrow C_2H_4 + O_2$ [*high]	$3.12 \times 10^{-13}$	0	30.0
$C_2H_4 + O_2(a^1\Delta_g) \rightarrow C_2H_4 + O_2$ [*exp. fit]	$5.46 \times 10^{-10}$	0	48.6
$C_2H_4 + O_2(a^1\Delta_g) \rightarrow C_2H_3 + HO_2$ [*]	$7.01 \times 10^{-11}$	0	146.5

**Table 9** Reaction rates of  $O_2(a^1\Delta_g)$  with hydrocarbon species. [\*low] = estimated rate with low activation energy, [\*high] = estimated rate with high activation energy, [\*exp. fit] = estimated rate with activation energy to fit trend of experimental results, [\*] = estimated rate.

The reactive and collisional quenching rates for some of the hydrocarbon species were added to the kinetic mechanism one at a time to test the sensitivity of flame speed enhancement. In **Table 9** is a list of the reactions along with their rates. Initially the reactions with  $CH_4$  of



were added but did not change the flame speed enhancement, which was reasonable considering the low concentrations of  $CH_4$  in the system. Next, noting that the inclusion of  $O_2(a^1\Delta_g)$  collisional quenching by the parent fuel  $H_2$  in an  $H_2$ - $O_2$  system via reaction (18) was found in previous numerical investigations to be significant and decreased the effectiveness of  $O_2(a^1\Delta_g)$  enhancement, it is reasonable to include collisional quenching by the parent fuel via



for our hydrocarbon fueled combustion system. Some collisional reaction rates for  $O_2(a^1\Delta_g)$  with  $C_2H_4$  and other small hydrocarbon fuels are known, but they are only at 298 K. To the authors knowledge, there are no verified quenching rates of hydrocarbon species (specifically  $C_2H_4$ ) with  $O_2(a^1\Delta_g)$  in the intermediate- to high-temperature range where they would be the most important for a flame system.

The work of Borrell and Richards found that the temperature dependence of  $O_2(a^1\Delta_g)$  quenching by  $H_2$  was approximately Arrhenius and that other species also follow an Arrhenius temperature dependence [69]. It was assumed that  $C_2H_4$  might also follow this temperature dependence for quenching  $O_2(a^1\Delta_g)$ . Originating with the quenching rate of  $O_2(a^1\Delta_g)$  by  $C_2H_4$  at 298 K, an Arrhenius temperature-dependent rate was estimated to explain the trend discrepancy shown in the experimental results of **Fig. 29**. Three different temperature dependencies were chosen with a range of activation energies. Previously published temperature-dependent collisional quenching rates of  $O_2(a^1\Delta_g)$  have shown that the activation energy range is typically

between 15 kJ/mole and 20 kJ/mole [55]. The activation energy for the collisional quenching of  $O_2(a^1\Delta_g)$  by  $H_2$  is as high as 32 kJ/mole; therefore, the range of 15-30 kJ/mole was chosen for the activation energies of reaction (21), with a reaction constant chosen in order to agree with published rates at 298 K. The envelope of reaction rates for reaction (22) using activation energies from 15 kJ/mole to 30 kJ/mole are shown in **Fig. 33** and are labeled as “Quenching A.”

Computations were performed using the rates within the envelope of “Quenching A” in **Fig. 33**, and the results are shown in **Fig. 34**. The flame speed enhancement decreased slightly but not enough to explain the discrepancy. In an attempt to explain the disagreement, a rate for reaction (20) was chosen in order to bring the enhancement by  $O_2(a^1\Delta_g)$  down to the enhancement by  $O_3$ . To match this result, a reaction constant of  $5.46 \times 10^{-10} \text{ cm}^3/\text{molecule/s}$  and an activation energy of 48.6 kJ/mole were chosen, with the temperature dependence shown in **Fig. 33** as “Quenching B.” By using the “Quenching B” rate for reaction (22), the results of enhancement by  $O_3$  and  $O_2(a^1\Delta_g)$  were approximately equal, thereby agreeing with the trends of the experimental results (**Fig. 34**). A rate of production analysis of  $O_2(a^1\Delta_g)$  was performed with the “Quenching B” rate and the major consumption pathway shifted to reaction (22) with negligible consumption by reaction (18). The concentration profile of  $O_2(a^1\Delta_g)$  showed a more rapid decrease in the earlier stages of the flame but with no

appreciable increase in  $C_2H_4$  consumption or O and OH production. Furthermore, the quenching pathway involved electronic-to-vibrational-translational energy transfer that releases so little energy that the translational temperature changed negligibly. The computed temperature profiles confirmed the negligible increase in temperature and therefore that a significant concentration of

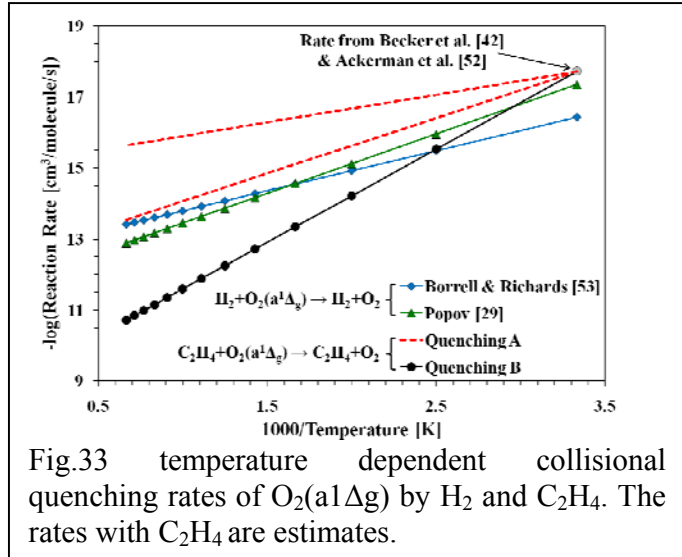


Fig.33 temperature dependent collisional quenching rates of  $O_2(a^1\Delta_g)$  by  $H_2$  and  $C_2H_4$ . The rates with  $C_2H_4$  are estimates.

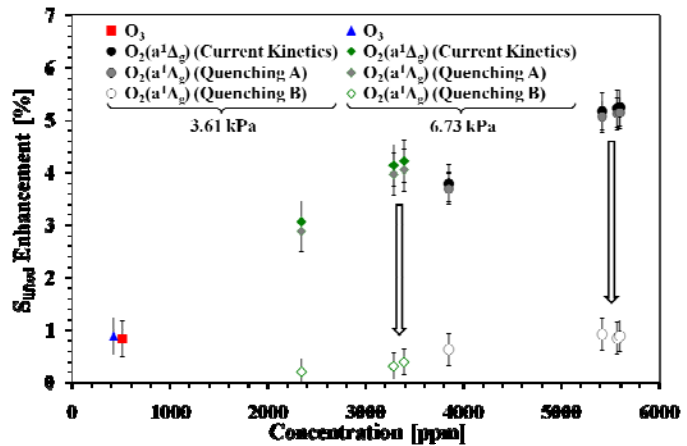


Fig.34 of computational results of lifted flame speed enhancement with  $O_2(a^1\Delta_g)$  and  $O_3$  using the estimated collisional quenching rate of  $C_2H_4$  with  $O_2(a^1\Delta_g)$  from Fig. 31. “Quenching A” = inclusion of temperature dependent quenching of  $O_2(a^1\Delta_g)$  by  $C_2H_4$  with  $E_a=30$  kJ/mol, “Quenching B” = inclusion of temperature dependent quenching of  $O_2(a^1\Delta_g)$  by  $C_2H_4$  to fit trend of experimental results. The error bars denote the variation in lifted flame speed enhancement when using different  $C_2H_4$  kinetic mechanisms.

$O_2(a^1\Delta_g)$  was consumed and did not affect the flame in the process. The high activation energy and hence strong temperature dependence of reaction (22), given by the estimated rate “Quenching B,” mitigated the computed enhancement discrepancy, but the rate appears unreasonably high and has not been validated and therefore requires further investigations.

The last possible explanation of the trend discrepancy in computed enhancement lies in the reactive quenching of  $O_2(a^1\Delta_g)$  by  $C_2H_4$  and its fragments. The first assumption was to decrease the activation energy of the reaction



by the energy contained within  $O_2(a^1\Delta_g)$ . This assumption equates to decreasing the activation energy by 0.98 eV (94.5 kJ/mole), and the rate is shown in **Table 9**. The inclusion of this reaction in the kinetic mechanism did not result in any change in flame speed enhancement because the rate is slow in comparison to other reaction pathways with  $C_2H_4$  and  $O_2(a^1\Delta_g)$ . Beyond reaction (23) there could be other possible product pathways that have been investigated through quantum calculations with  $C_2H_4$  [70,71]. The pathways show that  $O_2(a^1\Delta_g)$  can attack the double carbon bond to split the parent fuel molecule, possibly providing significant enhancement of fuel oxidation rates by producing  $CH_2O$  and other hydrocarbon fragments, but the rates are not known.

The results suggest that the probable reactive scheme has both collisional and reactive quenching of  $O_2(a^1\Delta_g)$  by the parent fuel and its fragments. There remain many unknowns as to the kinetic mechanisms for  $O_2(a^1\Delta_g)$  with hydrocarbons under flame conditions. The lack of rate data for these reactions in the intermediate- to high-temperature range that is applicable to combustion systems remains a significant obstacle and requires further investigation; nevertheless, the results from this investigation have provided the first experimental data set for flame propagation enhancement by  $O_2(a^1\Delta_g)$  that provides a foundation for future investigations.

### 2.3.3 Conclusions

The present study provides a promising approach to isolate plasma-produced excited species for the kinetic study of plasma-assisted combustion. By separating the plasma and combustion systems, specific plasma-produced species can be isolated and measured while minimizing the complications of other plasma-flame interactions. Isolation of the specific effects of individual plasma-produced species will have a significant impact on the development of detailed plasma-flame kinetic mechanisms. Through the current work a platform to study quantitatively the enhancement effects of plasma-produced  $O_2(a^1\Delta_g)$  on  $C_2H_4$  lifted flame propagation speeds was developed. It was found quantitatively, for the first time, that  $O_2(a^1\Delta_g)$  enhances flame propagation. The addition of NO to the plasma afterglow allowed for an order-of-magnitude increase in the  $O_2(a^1\Delta_g)$  concentration at a given residence time by removing the quenching species  $O_3$  and O. The NO was extremely effective because of the catalytic cycle to remove  $O_3$  and O, as well as having a negligible effect on flame speed. The  $O_2(a^1\Delta_g)$  was produced in concentrations of over 5000 ppm to enhance flame propagation of  $C_2H_4$  lifted flames by several percent at 3.61 kPa and 6.73 kPa pressures.

Numerical simulations using the state-of-the-art rates of the collisional and reactive quenching reactions have shown that there is a significant discrepancy in the predicted enhancement compared with the experimental data. The pathways of enhancement found in the simulations showed that the branching reaction of  $O_2(a^1\Delta_g)$  with H provided O and OH early in the reaction zone and increased chemical heat release and flame propagation speed. The lack of temperature-dependent quenching rate data of  $O_2(a^1\Delta_g)$  by hydrocarbon species was suspected to

be the main cause for the discrepancy. Estimations of the temperature dependent collisional quenching rate of  $O_2(a^1\Delta_g)$  by  $C_2H_4$  have shown good agreement with the experimental results trends, but the suggested rates appear unreasonably high and need to be validated in future studies. The reactive quenching pathways and their rates remain unknown; therefore, a combination of both the collisional and reactive quenching rates of  $O_2(a^1\Delta_g)$  with hydrocarbon species, specifically the parent fuel molecule, are required in order to explain combustion enhancement correctly. The experimental results therefore have provided the first data of the isolated effect of  $O_2(a^1\Delta_g)$  under flame conditions, which are of paramount importance for the development of reaction pathways and plasma-flame kinetic mechanisms. Future investigations are being targeted at establishing temperature-dependent quenching rates of  $O_2(a^1\Delta_g)$  to enable more accurate predictive modeling of the plasma-flame interaction.

The experimental results also imply that when energy is coupled into specific plasma-produced species, there is no requirement for the control of heat loss. If energy is coupled into a reactive flow to raise the translational gas temperature only, there needs to be careful thermal management. When energy is coupled into energy modes of specific species, no thermal management needs to be considered. The energy contained within the species can be transported for significant distances and residence times and can be extracted at the combustion reaction zone. The plasma power remained constant at 80 W for all conditions with  $O_3$  and/or  $O_2(a^1\Delta_g)$  in the current experiments; therefore, the energy coupled into the flow by the plasma was recovered at the flame. More  $O_2(a^1\Delta_g)$  was produced than  $O_3$  for the same plasma power because of the difference in energy to produce these species.

Lastly, in and immediately downstream of an oxygen plasma there would be both O and  $O_2(a^1\Delta_g)$  but no  $O_3$  since it is the product of a time-dependent recombination of O and  $O_2$ . The O atoms most likely will be more reactive, but there will be higher concentrations of  $O_2(a^1\Delta_g)$ . If oxygen plasma is located closer to a combustion reaction zone, the effects of  $O_2(a^1\Delta_g)$  can become more pronounced.

### 3.0 Participating Personnel

#### *Princeton University:*

Fully or Partially Supported by the Project: Professor Yiguang Ju, PI  
 Timothy Ombrello, graduate student  
 Zheng Chen, graduate student  
 Sanghee Won, Research staff  
 Jingning Shan, Research staff

#### *Drexel University:*

Fully or Partially Supported by the Project: Professor Alexander Fridman, co-PI  
 Professor Alexander Gutsol  
 Shailesh Gangoli, graduate student

## 4.0 Publications

### *Peer Reviewed Journal Publications*

1. Ombrello, T., Ju, Y., and Fridman, A., "Kinetic Ignition Enhancement of Diffusion Flames by Nonequilibrium Magnetic Gliding Arc Plasma," *AIAA Journal*, Vol. 46, No. 10, 2008, pp. 2424-2433.
2. Fridman, A., Gutsol, A., Gangoli, S., Ju, Y., and Ombrello, T., "Characteristics of Gliding Arc and its Application in Combustion Enhancement," *Journal of Propulsion and Power*, Vol. 24, No. 6, 2008, pp. 1216-1228.
3. Ombrello, T. and Ju, Y., "Kinetic Ignition Enhancement of H<sub>2</sub> versus Fuel-Blended Air Diffusion Flames Using Nonequilibrium Plasma," *IEEE Transactions on Plasma Science*, Vol. 36, No. 6, 2008, pp. 2924-2932, also presented at the 32<sup>nd</sup> Symp. Combustion.
4. Timothy Ombrello, Sang Hee Won, and Yiguang Ju, and Skip Williams, Flame Propagation Enhancement by Plasma Excitation of Oxygen Part I: Effects of O<sub>3</sub>, *Combustion and Flame*, in press, 2010.
5. Timothy Ombrello, Sang Hee Won, and Yiguang Ju, and Skip Williams, Flame Propagation Enhancement by Plasma Excitation of Oxygen Part II: Effects of O<sub>2</sub>(a<sup>1</sup>Δ<sub>g</sub>), *Combustion and Flame*, in press, 2010.
6. Zheng Chen, Michael P. Burke, Yiguang Ju, Effects of Lewis Number and Ignition Energy on the Determination of Laminar Flame Speed Using Propagating Spherical Flames, *Proc. Combust. Institute*, Volume 32, Issue 1, 2009, Pages 1253-1260.

### *Presentations at Conferences*

1. Ombrello, T., Ju, Y., and Fridman, A., "Investigation of Non-Equilibrium Plasma Induced Kinetic Ignition of Counterflow Diffusion Flames," AIAA-2008-1361, 46<sup>th</sup> AIAA Aerospace Sciences Meeting and Exhibit, 7-10 January 2008, Reno, Nevada.
2. Chen, Z., Burke, M., and Ju, Y., "Effects of Lewis Number on Spherical Flame Initiation," AIAA-2008-977, 46<sup>th</sup> AIAA Aerospace Sciences Meeting and Exhibit, 7-10 January 2008, Reno, Nevada.
3. Ombrello, T. and Ju, Y., "Studies of Ignition Enhancement Mechanisms of H<sub>2</sub> Versus Fuel-Blended-Air Diffusion Flames Using Non-Equilibrium Plasma," 32<sup>nd</sup> International Symposium on Combustion, The Combustion Institute, 3-8 August 2008, Montreal, Quebec, Canada.
4. Ombrello, T., Won, S.H., and Ju, Y., "Lifted Flame Speed Enhancement by Ozone," 4<sup>th</sup> International Workshop on Plasma-assisted Combustion, 16-19 September 2008, Falls Church, Virginia.
5. Ombrello, T., Won, S.H., Ju, Y., and Williams, S., "Lifted Flame Speed Enhancement by Plasma Excitation of Oxygen," AIAA-2009-0689, 47<sup>th</sup> AIAA Aerospace Sciences Meeting, 5-8 January 2009, Orlando, Florida.
6. Chen, Z., Burke, M., and Ju, Y., "Studies on the Critical Flame Radius and Minimum Ignition Energy for Spherical Flame Initiation," AIAA-2009-1184, 47<sup>th</sup> AIAA Aerospace Sciences Meeting, 5-8 January 2009, Orlando, Florida.
7. Zheng Chen, Michael Burke, Yiguang Ju, "Studies on the Critical Flame Radius and Minimum Ignition Energy for Spherical Flame Initiation," AIAA-2009-1184, 47<sup>th</sup> AIAA Aerospace Sciences Meeting, 2009.
8. Timothy Ombrello, Sang Hee Won, Yiguang Ju, "Enhancement of flame speed by plasma excitation of oxygen," Proceedings of the 6th U.S. National Combustion Meeting, 2009.
9. Timothy Ombrello, Wenting Sun, Sang Hee Won, Yiguang Ju, Skip Williams, Kihei, Maui, Campbell Carter, "Mechanisms of Kinetic Combustion Enhancement by O<sub>2</sub>(a<sup>1</sup>Δ<sub>g</sub>), AIAA-2010-1586, 48<sup>th</sup> AIAA Aerospace Sciences Meeting, 2010.

10. Wenting Sun, Timothy Ombrello, Sang Hee Won, Mruthunjaya Uddi, Yiguang Ju, "Effects of Non-Equilibrium Plasma on Counterflow Diffusion Flames," AIAA-2010-1331, 48th AIAA Aerospace Sciences Meeting, 2010.

## **5.0 Interactions and Consultations**

Professor Ju and Timothy Ombrello have been in collaboration with Professor Fridman and his associates Professor Gutsol and Shailesh Gangoli at the Drexel Plasma Institute of Drexel University on a regular basis. This interaction has allowed for a discussion and work forum to take the knowledge obtained via the analysis of the MGA plasma discharge and apply it to the knowledge of combustion to develop a model of the plasma/flame interaction.

Professor Ju, Dr. Sanghee Won and Timothy Ombrello have also worked with Dr. Skip Williams of the Air Force Research Laboratory at Wright-Patterson Air Force Base to design and develop a low pressure chamber to be used for combustion experiments to examine the effects of O<sub>3</sub> and singlet oxygen via the microwave plasma discharge on the flame propagation of hydrocarbon lifted flames.

Professor Ju and Timothy Ombrello have also worked closely with Dr. Campbell Carter of the Air Force Research Laboratory at Wright-Patterson Air Force Base to establish diagnostic capability of atomic oxygen measurements. Timothy Ombrello and Sanghee Won have traveled to Wright-Patterson Air Force Base twice to perform laser diagnostic measurements of OH PLIF, ozone, and singlet oxygen.

## **6.0 Honors and Awards**

- |           |   |
|-----------|---|
| May 2007  | Best Paper Award, The paper "Flammability Limit Extension of Non-Premixed Counterflow Flames via Stabilized Non-Equilibrium Plasma Gliding Arc" by T. Ombrello, X. Qin, Y. Ju and C. Carter and presented by my graduate student (T. Ombrello) at the Fifth Asia Pacific Conference on Combustion held at Adelaide of Australia in 2005, won the most outstanding paper prize for young researchers (the Young Investigator Award). |
| July 2008 | Zheng Chen, awarded the Bernard Lewis Fellowship from the International Combustion Institute<br>Tim Ombrello, the Wu Prize for Excellence in Research of Princeton University.  |

## **7.0 Inventions**

NA

## 8.0 References of This Report

---

- 1 E. Barbi, J. Mahan, W. O'Brien, T. Wagner, J. Prop. Power 5:2 (1989) 129-133.
- 2 I. Kimura, H. Aoki, M. Kato, Combust. Flame 42 (1981) 297-305.
- 3 K. Takita, A. Moriwaki, T. Kitagawa, G. Masuya, Combust. Flame 132:4 (2003) 679-689.
- 4 T. Wagner, W. O'Brien, G. E. Northam, J. Prop. Power 5:5 (1989) 548-554.
- 5 T. Ombrello, X. Qin, Y. Ju, A. Gutsol, A. Fridman, AIAA J. 44:1 (2006) 142-150.
- 6 T. Ombrello, Y. Ju, A. Fridman, AIAA J. 46:10 (2008) 2424-2433.
- 7 T. Ombrello, Y. Ju, IEEE Trans. Plasma Sci. 36:6 (2008) 2924-2932.
- 8 S. Bozhenkov, S. Starikovskaia, A. Y. Starikovskii, Combust. Flame 133 (2003) 133-146.
- 9 A. Starikovskii, Proc. Combust. Inst. 30 (2005) 2405-2417.
- 10 G. Lou, A. Bao, M. Nishihara, S. Keshav, Y. Utkin, J. Rich, W. Lempert, I. Adamovich, Proc. Combust. Inst. 31 (2007) 3327-3334.
- 11 S. Pancheshnyi, D. Lacoste, A. Bourbon, C. Laux, IEEE Trans. Plasma Sci. 34:6 (2006) 2478-2487.
- 12 H. Jagers, A. Von Engel, Combust. Flame 16 (1971) 275-285.
- 13 S. Won, M. Cha, C. Park, S. Chung, Proc. Combust. Inst. 31 (2007) 963-970.
- 14 S. Won, S. Ryu, M. Kim, M. Cha, S. Chung, Combust. Flame 152 (2008) 496-506.
- 15 I. Esakov, L. Grachev, K. Khodatev, V. Vinogradov, D. Van Wie, 44th AIAA Aerospace Sciences Meeting and Exhibit (2006) AIAA-2006-1212.
- 16 Y. Ju, S. Macheret, R. Miles, D. Sullivan, 40th AIAA/ASME/SAE/ASEE Joint Propulsion Conference and Exhibit (2004) AIAA-2004-2721.
- 17 S. Zaidi, S. Macheret, L. Vasilyak, R. Miles, Y. Ju, D. Sullivan, 35th AIAA Plasmadynamics and Lasers Conference (2004) AIAA-2004-3707.
- 18 C. Cathey, J. Cain, H. Wang, M. Gunderson, C. Carter, M. Ryan, Combust. Flame 154 (2008) 715-727.
- 19 I. Kosarev, N. Aleksandrov, S. Kindysheva, S. Starikovskaia, A. Starikovskii, J. Prop. Power 24:6 (2008) 1182-1197.
- 20 E. Stockman, S. Zaidi, R. Miles, C. Carter, M. Ryan, Combust. Flame 156 (2009) 1453-1461.
- 21 S. Starikovskaia, J. Phys. D: Appl. Phys. 39 (2006) R265-R299.
- 22 M. Uddi, N. Jiang, E. Mintusov, I. Adamovich, W. Lempert, Proc. Combust. Inst. 32 (2009) 929-936.
- 23 V. Golovitchev, J. Chomiak, Combust. Sci. Tech. 135:1-6 (1998) 31-47.
- 24 H. Nishida, T. Tachibana, J. Prop. Power 22:1 (2006) 151-157.
- 25 T. Nomaguchi, S. Koda, Proc. Combust. Inst. 22:1 (1988) 1677-1682.
- 26 T. Tachibana, H. K, H. Nishida, H. Osada, Combust. Flame 85:3-4 (1991) 515-519.
- 27 H. Yamada, M. Yoshii, A. Tezaki, Proc. Combust. Inst. 30:1 (2005) 2773-2780.
- 28 D. Lucas, D. Dunn-Rankin, K. Hom, N. Brown, Combust. Flame 69:2 (1987) 171-184.
- 29 B. Lukhovitskii, A. Starik, N. Titova, Combust. Expl. Shock Waves 41:4 (2005) 386-394.



- 
- 30 A. Starik, B. Lukhovitsky, N. Titova, J. Russian Laser Research 27:6 (2006) 533-551.
- 31 M. Gluckstein, R. Morrison, T. Khammash, (1955) Combustion with Ozone-Modification of Flame Speeds C2 Hydrocarbon-Air Mixtures, University of Michigan.
- 32 A.A. Ionin, I.V. Kochetov, A.P. Napartovich, N.N. Yuryshev, J. Phys. D: Appl. Phys. 40 (2007) R25-R61.
- 33 A. Starik, N. Titova, Kinet. Catal. 44:1 (2003) 28-39.
- 34 A. Starik, N. Titova, L. Bezgin, V. Kopchenov, V. Naumov, Czech. J. Phys. 56 (2006) B1357-B1363.
- 35 A. Starik, N. Titova, L. Bezgin, V. Kopchenov, V. Naumov, Czech. J. Phys. 56 (2006) B1357-B1363.
- 36 A. Starik, P. Kuleshov, N. Titova, Tech. Phys. 53:2 (2008) 235-243.
- 37 V. Kozlov, A. Starik, N. Titova, Combust. Expl. Shock Waves 44:4 (2008) 371-379.
- 38 A. Bourig, D. Thevenin, J. Martin, G. Janiga, K. Zahringer, Proc. Combust. Inst. 32 (2009) 3171-3179.
- 39 G. Smekhov, L. Ibraguimova, S. Karkach, O. Skrebkov, O. Shatalov, High Temp. 45:3 (2007) 395-407.
- 40 G. Smekhov, L. Ibraguimova, S. Karkach, O. Skrebkov, O. Shatalov, High Temp. 45:3 (2007) 395-407.
- 41 O. Skrebkov, S. Karkach, Kinet. Catalysis 48:3 (2007) 367-375.
- 42 V. Smirnov, O. Stelmakh, V. Fabelinsky, D. Kozlov, A. Starik, N. Titova, J. Phys. D - Appl. Phys. 41:19 (2008) .
- 43 A. Starik, B. Lukhovitskii, V. Naumov, N. Titova, Tech. Phys. 52 (2007) 1281-1290.
- 44 A. Starik, N. Titova, Doklady Phys. 46 (2001) 627-632.
- 45 Li, J., Zhao, Z., Kazakov, A., and Dryer, F.L., "An Updated Comprehensive Kinetic Model of Hydrogen Combustion," International Journal of Chemical Kinetics, 36 (2004) 1-10.
- 46 Mueller, M.A., Yetter, R.A. and Dryer, F.L., "Kinetic Modeling of the CO/H<sub>2</sub>O/O<sub>2</sub>/NO/SO<sub>2</sub> System: Implications for High-Pressure Fall-off in the SO<sub>2</sub> + O(+M) = SO<sub>3</sub>(+M) Reaction," International Journal of Chemical Kinetics, 30 (2000) 317-339.
- 47 Zhao, Z., Chaos, M., Kazakov, A., and Dryer, F.L., "Thermal Decomposition Reaction and a Comprehensive Kinetic Model of Dimethyl Ether," International Journal of Chemical Kinetics, 40 (2008) 1-18.
- 48 Bowman et al., GRI-Mech Homepage, Gas Research Institute, Chicago, 1994, URL:[http://www.me.berkeley.edu/gri\\_mech/](http://www.me.berkeley.edu/gri_mech/).
- 49 Chen, Z., Qin, X., Ju, Y., Zhao, Z., Chaos, M., and Dryer, F.L., "High Temperature Ignition and Combustion Enhancement by Dimethyl Ether Addition to Methane-Air Flames," Proceedings of the Combustion Institute, Thirty-First International Symposium on Combustion, 31 (2007) 1215-1222.
- 50 Langille, J.A., Dong, Y., Andac, M.G., Egolfopoulos, F.N., and Tsotsis, T.T., "Non-Premixed Ignition by Vitiated Air in Counterflow Configurations," Combustion Science and Technology, 178:4 (2006) 635-653.
- 51 J. Malicet, D. Daumont, J. Charbonnier, C. Parisse, A. Chakir, J. Brion, J. Atm. Chem. 21:3 (1995) 263-273.

- 
- 52 S. Chung, Proc. Combust. Inst. 31:1 (2007) 877-892.
- 53 S. Chung, Proc. Combust. Inst. 31:1 (2007) 877-892.
- 54 J. Lee, S. Won, S. Jin, S. Chung, Combust. Flame 135:4 (2003) 449-462.
- 55 Y. Ju, Y. Xue, Proc. Combust. Inst. 30 (2005) 295-301.
- 56 Y. Xue, Y. Ju, Combust. Sci. Tech. 178 (2006) 2219-2247.
- 57 M. Kim, S. Won, S. Chung, Proc. Combust. Inst. 31 (2007) 901-908.
- 58 G. Ruetsch, L. Vervisch, A. Linan, Phys. Fluids 7 (1995) 1447-1454.
- 59 PREMIX from the CHEMKIN Package, Reaction Design, 6440 Lusk Boulevard, Suite D-205 San Diego, CA 92121, [www.reactiondesign.com](http://www.reactiondesign.com).
- 60 L. Ibraguimova, G. Smekhov, O. Shatalov, Recommended Rate Constants of Chemical Reactions in an H<sub>2</sub>-O<sub>2</sub> Gas Mixture with Electronically Excited Species O<sub>2</sub>(1Δ), O(1D), OH(2Σ) Involved, Institute of Mechanics of Lomonosov, Moscow State University (2003).
- 61 G. Smekhov, L. Ibraguimova, S. Karkach, O. Skrebkov, O. Shatalov, High Temp. 45:3 (2007) 395-407.
- 62 Z. Qin, V. Lissianski, H. Yang, W. Gardiner, S. Davis, H. Wang, Proc. Combust. Inst. 28:2 (2000) 1663-1669.
- 63 R. Morrissey, C. Schubert, Combust. Flame 7:3 (1963) 263-268.
- 64 S. Williams, M. Gupta, T. Owano, D. Baer, A. O'Keefe, D. Yarkony, S. Matsika, Opt. Lett. 29:10 (2004) 1066-1068.
- 65 H. Wang, A. Laskin, Internal Report, 1998.
- 66 H. Wang, X. You, A.V. Joshi, S.G. Davis, A. Laskin, F. Egolfopoulos, C.K. Law, USC Mech Version II. High-Temperature Combustion Reaction Model of H<sub>2</sub>/CO/C<sub>1</sub>-C<sub>4</sub> Compounds, [http://ignis.usc.edu/USC\\_Mech\\_II.htm](http://ignis.usc.edu/USC_Mech_II.htm), May 2007.
- 67 L. Ibraguimova, G. Smekhov, O. Shatalov, Recommended Rate Constants of Chemical Reactions in an H<sub>2</sub>-O<sub>2</sub> Gas Mixture with Electronically Excited Species O<sub>2</sub>(1Δ), O(1D), OH(2Σ) Involved, Institute of Mechanics of Lomonosov, Moscow State University (2003).
- 68 R.A. Ackerman, J.N. Pitts, R.P. Steer, J. Chem. Phys. 52 (1970) 1603-1604.
- 69 P. Borrell, D.S. Richards, J. Chem. Soc., Faraday Trans. 2 85:9 (1989) 1401-1411.
- 70 M. Hotokka, B. Roos, P. Siegbahn, J. Amer. Chem. Soc. 105:16 (1983) 5263-5269.
- 71 Y. Yoshioka, T. Tsunesada, K. Yamaguchi, I. Saito, International J. Quant. Chem. 65 (1997) 787-801.